On the non-self-adjoint and multiscale character of passive scalar mixing under laminar advection

Miguel A. Jiménez-Urias† and Thomas W. N. Haine
Earth and Planetary Sciences, Johns Hopkins University, Baltimore, MD 21218, USA

(Received xx; revised xx; accepted xx)

Except in the trivial case of spatially uniform flow, the advection-diffusion operator of a passive scalar tracer is linear and non-self-adjoint. In this study, we exploit the linearity of the governing equation and present an analytical eigenfunction approach for computing solutions to the advection-diffusion equation in two dimensions given arbitrary initial conditions, and when the advecting flow field at any given time is a plane parallel shear flow. Our analysis illuminates the specific role that the non-self-adjointness of the linear operator plays in the solution behavior, and highlights the multiscale nature of the scalar mixing problem given the explicit dependence of the eigenvalue-eigenfunction pairs on a multiscale parameter $q = 2ikPe$, where k is the non-dimensional wavenumber of the tracer in the streamwise direction and Pe is the Péclet number. We complement our theoretical discussion on the spectra of the operator by computing solutions and analyzing the effect of shear flow width on the scale-dependent scalar decay of tracer variance, and characterize the distinct self-similar diffusive processes that arise from the shear flow dispersion of an arbitrarily compact tracer concentration. Lastly, we discuss limitations of the present approach and future directions.

1. Introduction

Stirring and mixing results from the combined action of differential advection and molecular diffusion on a material quantity (Thiffeault 2008), and is a ubiquitous process in geophysical, environmental, and industrial fluids (see for example Biferale *et al.* 1995; Faller & Auer 1988; Seo & Cheong 1998; Haynes & Shuckburgh 2000; Neuman & Tartakovsky 2009; Boano *et al.* 2014; Van Sebille *et al.* 2018). Despite its importance, a complete analytical description of stirring and mixing remains an open problem owing to the complex interplay between differential advection, diffusion and the multiscale nature of the problem, highlighted by the multifractal behavior that the scalar field exhibits even when advection is a spatially smooth function of space usually a single Fourier mode (Aref 1984; Pierrehumbert 1994; Antonsen Jr *et al.* 1996; De Moura 2014).

The evolution of a scalar tracer under the combined effect of molecular mixing and stirring is given by the advection-diffusion equation, written in the absence of sources and sinks as

$$\frac{\partial \theta}{\partial t} + \mathbf{u} \cdot \nabla \theta = \kappa \nabla^2 \theta, \tag{1.1}$$

where κ is the molecular diffusivity and $\mathbf{u}$ is a time-varying, non-divergent velocity field. The tracer concentration θ is considered dynamically-passive when its evolution has no effect on the inertia of the flow so that the velocity $\mathbf{u}$ is prescribed (although $\mathbf{u}$ need not solve the Navier-Stokes equations; Majda & Kramer 1999). From a theoretical

---

† Email address for correspondence: mjimen17@jhu.edu

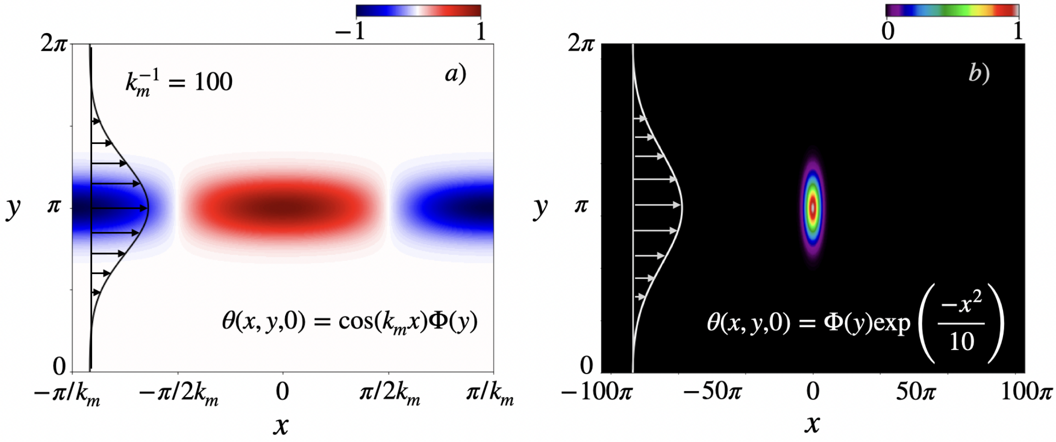

FIGURE 1. The two initial conditions considered in this study: a) A single along-stream mode, with arbitrary cross-stream initial structure, and b) a localized concentration patch centered at $x = 0$. Both types of initial condition are related due to the linearity of the governing equations. Note that the Gaussian function $\Phi(y)$ is centered at $y = \pi$ in both cases, although it is not a requirement for our analysis. The domain is identical in both cases.

point of view, equation (1.1) provides the simplest example of a linear non-self-adjoint operator, which is ubiquitous in many physical sciences (Miri & Alu 2019), and whose qualitative properties are not fully understood (Childress & Gilbert 1995; Sukhatme & Pierrehumbert 2002; Giona *et al.* 2004). Furthermore, the study of stirring and mixing via (1.1) offers many of the same mathematical challenges as the study of fluid turbulence while remaining a linear and therefore less complicated physical model (Pierrehumbert 2000).

In this study we compute the spectra of the operator (1.1) and use it to study the property and behavior of analytical solutions in a doubly-periodic domain with arbitrary initial conditions. We focus on steady shear flows, as these represent a building block for more complex planar flow fields relevant to a wide range of applications involving flow fields that can be defined by

$$\mathbf{u}(\mathbf{x},t) = U_0 \begin{cases} U(y+\xi)\,\hat{\mathbf{i}}, & \text{if} \quad nT < t < nT + T/2 \\ V(x+\xi)\,\hat{\mathbf{j}}, & \text{if} \quad nT + T/2 < t < (n+1)T, \end{cases} \tag{1.2}$$

where T is the period, $n = 0, 1, \cdots$, ξ is a random variable and U_0 is the maximum flow amplitude †, and U, V are the integrable functions of their spatial coordinate. The flow (1.2) defines a wide class of flows that are of geophysical and theoretical relevance, and have been used extensively in the literature. Among those are the time-oscillating shear flows when U_0 time-periodic, ξ constant and $T \to \infty$ (see Zel'dovich 1982; Young *et al.* 1982); and the two-dimensional alternating flows characterized by chaotic advection with U_0 constant, $U = V$ a smooth spatial function and $\xi \in [0, 2\pi]$ a random variable (see Ottino 1990; Shaw *et al.* 2007; Fereday & Haynes 2004; Antonsen Jr *et al.* 1996; Pierrehumbert 2000; Vanneste 2006; Keating *et al.* 2010).

The ability to compute analytical solutions to (1.1) given a general initial condition has practical implications to the study of scalar mixing, since an arbitrary stage of the tracer evolution can be achieved via single time evaluation without the need to evolve

---

† In this paper, we fix U_0 to a constant value but it can be generally be considered a piece-wise constant.

intermediate steps, thus bypassing great computational and numerical constraints. The method described in this study allows the computation of tracer solutions that can be evolved from arbitrarily small scales until reaching the final late stage described by Taylor's dispersion (a clear distinction with the Ranz transform approach in Young *et al.* 1982; Meunier & Villermaux 2010). Applying the method described in this paper, allows us to improve upon the description of the multiscale scalar decay of tracer variance for a wide range of shear flows. We also expand upon the analysis with a detailed description of the distinct time-varying stages of shear flow dispersion in the context of strong and weakly self-similar processes for an arbitrarily compact tracer concentration (Castiglione *et al.* 1999; Ferrari *et al.* 2001; Latini & Bernoff 2001), and identify a shear flow that can be completely characterized by a Levy process (Levy walk) (Dubkov *et al.* 2008; Zaburdaev *et al.* 2015). For this reasons, this paper advances both theoretical and practical knowledge to the problem of tracer evolution described by the advection-diffusion equation.

The organization of the paper is as follows: In §2.1 we pose the mathematical problem, and in §2.2 we describe the method of solution to compute both eigenvalues and eigenfunctions of the associated non-self-adjoint operator. This allows us to compute solutions given general initial conditions that are valid for any $t > 0$. In §3 we analyze the behavior of solutions, focusing first on scale-dependent scalar decay, and then on the time-varying, shear dispersion properties of a localized tracer patch. In §4 we discuss advantages over other methods, as well as the ability to expand our analysis to more complex flows and boundary conditions, and in §5 we summarize results and future directions.

2. Analytical Solutions

2.1. *Problem statement*

Consider the governing equation (1.1) over a time interval t in which the velocity field (1.2) is a parallel shear flow of arbitrary amplitude U_0, say $\mathbf{u}(\mathbf{x},t) = U_0(U(y),0)$, in a doubly-periodic domain defined as $(-L/2 \leqslant x \leqslant L/2) \times (0 \leqslant y \leqslant M)$, with $L \geqslant M$.

We introduce the following non-dimensionalization

$$(x,y) = \left[\frac{M}{2\pi}\right](x^*,y^*), \quad \mathbf{u} = [U_0]\mathbf{u}^*, \quad t = [t_d]\,t^*, \tag{2.1}$$

where we choose M as the single lengthscale, and time is non-dimensionalized by the diffusive timescale $t_d = M^2/(4\pi^2\kappa)$. As a result, the non-dimensional governing equation (1.1) becomes (dropping the stars so that from now on we assume all variables are normalized)

$$\frac{\partial\theta}{\partial t} + Pe\,U(y)\frac{\partial\theta}{\partial x} = \nabla^2\theta. \tag{2.2}$$

This equation has been studied extensively for a wide range of shear flows (see Eckart 1948; Young *et al.* 1982; Majda & Kramer 1999; Vanneste 2006; Camassa *et al.* 2010). The Péclet number Pe is

$$Pe = \frac{U_0 M}{2\pi\kappa}, \tag{2.3}$$

and can be interpreted as the ratio of advective to diffusive timescales $(2\pi U_0 t_d/M)$ (Rhines & Young 1983). It represents the relative importance of the advective to diffusive tracer fluxes so that a large Péclet number implies weakly diffusive flows. We consider Pe an arbitrary parameter that can take any value and this implicitly allows U_0 to be time-dependent† when acting on a Fourier tracer mode. Note that both t_d and Pe are domain-scale quantities, independent of the scale of the shear flow, as both are defined with M as opposed to the intrinsic length-scale of the flow.

Our choice of a single lengthscale M in (2.1) implies the (non-dimensional) doubly-periodic boundary conditions

$$\theta(k_m x - \pi, y, t) = \theta(k_m x + \pi, y, t), \qquad \theta(x, y + 2\pi, t) = \theta(x, y, t). \tag{2.4}$$

where $k_m = M/L$ determines the aspect ratio of the gravest mode that fills the domain (i.e, when $k_m = 1$ the domain is a square). The value of k_m is arbitrary and can be made sufficiently small so that the domain approximates a semi-infinite rectangular domain. Our domain choice further implies any Fourier decomposition in the cross-stream direction is quantized (i.e., individual modes are $l = 0, \pm 1, \pm 2, \cdots$) while in the streamwise direction $k = jk_m$, with $j = 0, \pm 1, \pm 2, \cdots$.

In general, we are interested in initial conditions that can be expressed via Fourier decomposition as follows

$$\theta(x, y, 0) = \sum_i f_i(x)\Phi_i(y), \tag{2.5}$$

where each of $f_i(x)$ and $\Phi_i(y)$ are integrable functions in the space of $2\pi-$periodic functions.

We consider shear flows defined by an even Fourier series of the form

$$U(y) = \frac{\alpha_0}{2} + \sum_{m=1}^{\infty} \alpha_m \cos{(my)}. \tag{2.6}$$

We introduce an inverse width parameter L_d that controls the width of a shear flow while keeping intact the shear topology for example, piecewise constant and piecewise linear shear flows (see Fig. 2a–b, also Appendix A). Some of the shear flows considered here are idealized in their velocity gradient, e.g., piecewise constant or concentrated shear. These features represent some aspects of environmental flows whose spatial structure is sensitive to sampling, domain size and background noise. That is, in practice, real flows are patchy, localized and irregular in both time and space. Hence, our approach can compute solutions for flows with a discrete, wide spectrum (i.e., $\alpha_m \neq 0$ for arbitrary $m > 0$), a feature with theoretical and practical advantages.

An important global property of some shear flows is a symmetry after a translation in y and reflection in flow amplitude, i.e., a *shift-reflect* symmetry, defined mathematically as

$$U^*(y - \pi/P) = -U^*(y), \tag{2.7}$$

where $U^* = U - \alpha_0/2$ is the streamline velocity minus its spatial average, and $P = 1, 2, \cdots$ is the *periodicity* of the shear flow maxima within the finite domain (see Fig. 2). A shear flow that is shift-reflect symmetric has a Fourier series such that

$$U^*(y) = \sum_{m=1}^{\infty} \alpha_{P(2m-1)} \cos{[P(2m-1)y]}. \tag{2.8}$$

For example, the simplest case of a shift-reflect symmetric flow is $U^* = -(1/2)\cos(y)$. We emphasize that this is a global (domain-scale) property of the flow, independent of Pe, scale and topology of the velocity gradient, and therefore can describe properties of tracer evolution beyond oft-isolated streamlines where shear vanishes.

---

† Since U_0 can be considered piece-wise constant.

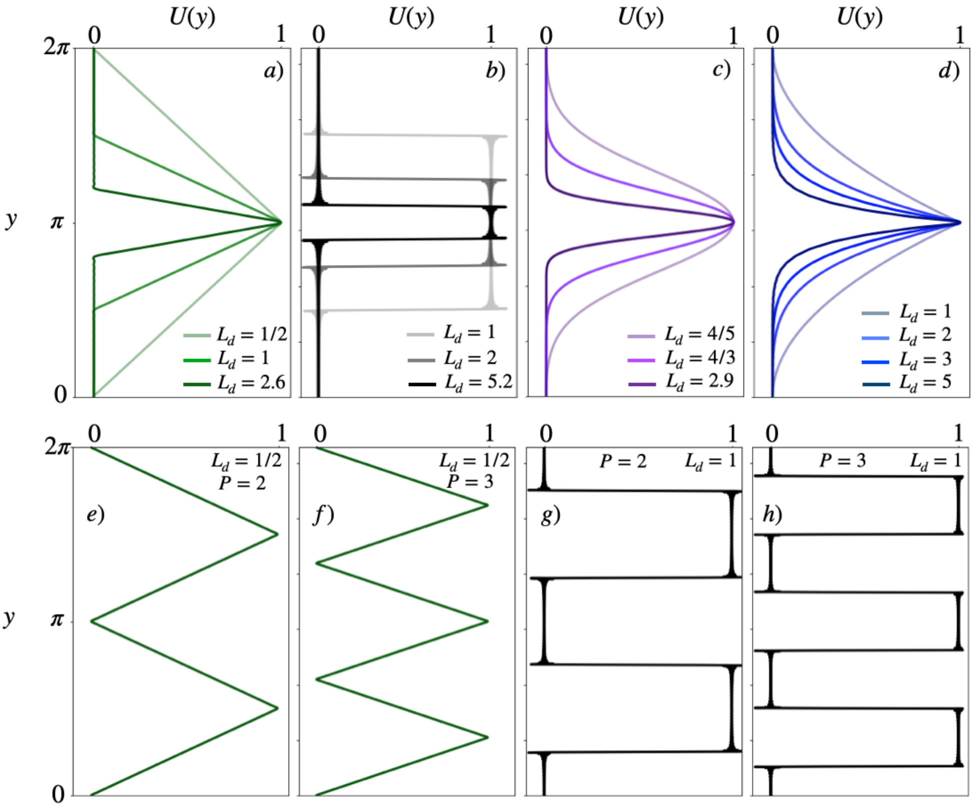

FIGURE 2. Shear flows $U(y)$, specifically, the a) triangular, b) square, c) Gaussian, and d) polynomial shear flows. The flow widths decrease as L_d increases and as $L_d \to \infty$ the shear flows all converge to the same flow, namely, $U = 1$ at $y = \pi$, $U = 0$ everywhere else. Panels e)–h) are triangular and square shear flows, as in a) and b), except they have higher $y-$periodicity P (repeated extrema). See Appendix A for the analytic definitions of the shear flow profiles.

2.2. *Method of solution*

Following Camassa *et al.* (2010), we take advantage of the linearity of the governing equation (2.2), the fact that the advection term is $x-$independent and consider a separable initial condition for each mode k in the streamwise direction of the form

$$\theta(x, \tilde{y}, t) = \Re\left\{\sum_{n=0}^{\infty} \chi_{2n}\, \phi_{2n}(\tilde{y}) \exp\left[ikx - \omega_{2n} t\right]\right\}, \tag{2.9}$$

where $2\tilde{y} = y$ is a scaled coordinate, $\phi_{2n}(\tilde{y})$ are eigenfunctions, and ω_{2n} are the associated eigenfrequencies. The coefficients to be determined, χ_{2n}, ensure that the solution satisfies the initial condition (2.5) . Substituting (2.9) into (2.2) shows that each eigenfunction satisfies the eigenvalue equation

$$\frac{d^2\phi_{2n}}{d\tilde{y}^2} + \left[a_{2n} - 2qU^*(2\tilde{y})\right]\phi_{2n} = 0. \tag{2.10}$$

Notice that (2.10) is written with the scaled independent variable $\tilde{y} = y/2$ to adhere to convention, as it is a type of Hill's equation (see Magnus & Winkler 2013 Ch. 5, also Strutt 1948). When the velocity is the zero-mean, non-normalized cosine shear flow, i.e., $U(2\tilde{y}) = \cos(2\tilde{y})$, (2.10) becomes the canonical Mathieu equation (McLachlan 1947; Olver *et al.* 2010).

Equation (2.10) is an eigenvalue problem that depends on the compound, multiscale parameter

$$q = 2ikPe. \tag{2.11}$$

This parameter contains the relevant physics of the system, and controls the multiscale, spatial, and temporal behavior of the solutions. From the eigenvalue $a_{2n}(q)$, the dispersion relation associated with each eigenfunction is given by

$$\omega_{2n} = \frac{a_{2n}(q) + \alpha_0 q}{4} + k^2. \tag{2.12}$$

The term k^2 represents pure diffusion of a normal mode in the $x-$ direction, and the eigenvalue $a_{2n}(q)$, which encodes the effect of varying shear in the y-direction at that scale, determines the relative contribution of the eigenfunction ϕ_{2n} to the tracer evolution in the $y-$ direction. The eigen-pair $\{a_{2n}, \phi_{2n}\}$ encode the effect of shear in the tracer evolution in the cross-stream direction at the scale k^{-1}.

To calculate the eigenfunctions we first follow a standard approach when solving Hill's equation (see, for example, McLachlan 1947 Ch.VI or Olver *et al.* 2010). Consider an eigensolution of (2.10) of the form

$$\phi_{2n} = \exp(\mu\tilde{y}) \sum_{r=-\infty}^{\infty} C_{2r}^{(2n)} \exp(2ri\tilde{y}), \tag{2.13}$$

where μ is the Floquet exponent and $\exp(\mu\tilde{y})$ is the Floquet multiplier. In general, all of μ, a_{2n}, and $C_{2r}^{(2n)}$ need to be determined (McLachlan 1947; Magnus & Winkler 2013). However, as restrict to $\pi-$periodic solutions which simplifies to $\mu \equiv 0$ (a different value of μ results in quasi-periodic solutions). Writing the cosine Fourier series in (2.6) as a sum of complex exponentials (with the property $\alpha_{-m} = \alpha_m$), and substituting (2.13) into (2.10) yields the following equation

$$\begin{aligned}\sum_{r=-\infty}^{\infty} C_{2r}^{(2n)} \Big(\Big[(2ri)^2 + a_{2n}\Big] \exp(2ri\tilde{y}) - \\ q\Big[\alpha_1\Big\{\exp[2(r+1)i\tilde{y}] + \exp[2(r-1)i\tilde{y}]\Big\} + \\ \alpha_2\Big\{\exp[2(r+2)i\tilde{y}] + \exp[2(r-2)i\tilde{y}]\Big\} + \\ \alpha_3\Big\{\exp[2(r+3)i\tilde{y}] + \exp[2(r-3)i\tilde{y}]\Big\} + \cdots\Big]\Big) = 0.\end{aligned} \tag{2.14}$$

Iterating over all possible values of r and equating to zero the coefficients multiplying each exponential of arbitrary order $R \in r$, we get the $R-$coefficient recursive equation

$$\Big[(2Ri)^2 + a_{2n}\Big] C_{2R}^{(2n)} = q \sum_{m=-\infty}^{\infty} \alpha_m C_{2(R+m)}^{(2n)}, \tag{2.15}$$

where the $m = 0$ term is not included in the sum on the right hand side as α_0 is already incorporated in the eigenvalue via (2.12). Equation (2.15) is almost identical to that studied by Hill in the lunar perigee problem (Hill 1886; McLachlan 1947).

Now split into even and odd $\pi-$periodic eigenfunctions. We define even eigenfunctions as

$$\phi^e_{2n}(q,\tilde{y}) = \sum_{r=0}^{\infty} A^{(2n)}_{2r}(q)\cos{(2r\tilde{y})}, \tag{2.16}$$

with $A^{(2n)}_0 = C^{(2n)}_0$ and $A^{(2n)}_{2r} = 2C^{(2n)}_{2r}$, $r = \pm 1, \pm 2, \cdots$. These eigenfunctions belong to a class of *cosine elliptic* functions given their dependence on an *eccentricity* parameter q, and when $q = 0$ the eigenfunctions reduce to multiples of $\cos{(ny)}$ (McLachlan 1947; Arscott 2014).

Similar to the approach by Chaos-Cador & Ley-Koo (2002), we cast the bi-infinite recursive equations (2.15) in matrix form as

$$\mathbf{T}^e \mathrm{X}^e_{2n} = a_{2n}\mathrm{X}^e_{2n}, \tag{2.17}$$

where the eigenvectors are

$$\mathrm{X}^e_{2n} = \left[\sqrt{2}A^{(2n)}_0, A^{(2n)}_2, \cdots, A^{(2n)}_{2R}, \cdots\right]^T, \tag{2.18}$$

and the superscript T implies transpose. Note that the elements of the eigenvector X^e_{2n} are the Fourier coefficients $A^{(2n)}_{2r}$ in (2.16). The vector satisfies an indefinite norm (as in the case of Mathieu's equation, see Brimacombe *et al.* 2021) given by

$$2\left[A^{(2n)}_0\right]^2 + \sum_{r=1}^{\infty}\left[A^{(2n)}_{2r}\right]^2 = 1, \tag{2.19}$$

and a further orthonormality relationship between the Fourier coefficients (Seeger 1997; Ziener *et al.* 2012)

$$\sum_{n=0}^{\infty} A^{(2n)}_{2r} A^{(2n)}_{2r'} = \delta_{rr'} - \frac{\delta_{0r}\delta_{0r'}}{2} \quad \text{for} \;\; r, r' = 0, 1, 2\cdots \tag{2.20}$$

with Kronecker delta $\delta_{rr'}$. The bi-infinite matrix $\mathbf{T}^e$ associated with (2.16) is

$$\mathbf{T}^e = \begin{bmatrix} 0 & \sqrt{2}q\alpha_1 & \sqrt{2}q\alpha_2 & \cdots & \sqrt{2}q\alpha_R & \cdot \\ \sqrt{2}q\alpha_1 & 4+q\alpha_2 & q(\alpha_1+\alpha_3) & \cdots & q(\alpha_{R-1}+\alpha_{R+1}) & \cdot \\ \sqrt{2}q\alpha_2 & q(\alpha_1+\alpha_3) & 16+q\alpha_4 & \cdot & \cdot & \cdot \\ \sqrt{2}q\alpha_3 & q(\alpha_2+\alpha_4) & q(\alpha_1+\alpha_5) & \ddots & \cdot & \cdot \\ \vdots & \vdots & \ddots & \ddots & \vdots & \cdot \\ \vdots & \vdots & \ddots & \ddots & q(\alpha_1+\alpha_{2R-1}) & \cdot \\ \sqrt{2}q\alpha_R & q(\alpha_{R-1}+\alpha_{R+1}) & \cdots & q(\alpha_1+\alpha_{2R-1}) & 4R^2+q\alpha_{2R} & \cdot \\ \cdot & \cdot & \cdot & \cdot & \cdot & \cdot \end{bmatrix}. \tag{2.21}$$

Odd eigenfunctions satisfy the same equation as in (2.10), but the nomenclature changes with $b_{2n+2}(q)$ now indicating the odd eigenvalue (see Arscott 2014). The odd (*sine elliptic*) eigenfunctions are defined as

$$\phi^o_{2n+2}(q,\tilde{y}) = \sum_{r=0}^{\infty} B^{(2n+2)}_{2r+2}\sin{[(2r+2)\tilde{y}]}. \tag{2.22}$$

When $q = 0$, these eigenfunctions reduce to multiples of $\sin{[(n+1)y]}$. The coefficients satisfy the normalization under an indefinite norm

$$\sum_{r=0}^{\infty}\left[B_{2r+2}^{(2n+2)}\right]^2=1, \tag{2.23}$$

and the orthonormalization

$$\sum_{n=0}^{\infty}B_{2r+2}^{(2n+2)}B_{2r'+2}^{(2n+2)}=\delta_{rr'}, \quad \text{for } \; r,r'=0,1,2\cdots \tag{2.24}$$

Similar to (2.17), the matrix equation for the odd eigenfunction-eigenvalue pair is

$$\mathbf{T}^o\mathrm{X}_{2n+2}^o=b_{2n+2}\mathrm{X}_{2n+2}^o, \tag{2.25}$$

where

$$\mathrm{X}_{2n+2}^o=\left[B_2^{(2n+2)},B_4^{(2n+2)},\cdots,B_{2R+2}^{(2n)},\cdots\right]^T. \tag{2.26}$$

The odd, bi-infinite matrix is

$$\mathbf{T}^o=\begin{bmatrix} 4-q\alpha_2 & q(\alpha_1-\alpha_3) & q(\alpha_2-\alpha_4) & \cdots & \cdot & \cdot \\ q(\alpha_1-\alpha_3) & 16-q\alpha_4 & q(\alpha_1-\alpha_5) & \cdots & \cdot & \cdot \\ q(\alpha_2-\alpha_4) & q(\alpha_1-\alpha_5) & 36-q\alpha_6 & \cdots & \cdot & \cdot \\ \vdots & \vdots & \vdots & \ddots & q(\alpha_1-\alpha_{2R-1}) & \cdot \\ q(\alpha_{R-1}-\alpha_{R+1}) & \cdots & \cdots & q(\alpha_1-\alpha_{2R-1}) & 4R^2-q\alpha_{2R} & \cdot \\ \cdot & \cdot & \cdot & \cdot & \cdot & \cdot \end{bmatrix}. \tag{2.27}$$

From matrices (2.21) and (2.27) the eigenvalue-eigenfunction pairs $\{a_{2n}(q),\mathbf{X}_{2n}^e(q)\}$ and $\{b_{2n+2}(q),\mathbf{X}_{2n+2}^o(q)\}$ are determined, and with them the associated eigenfunctions $\phi_{2n}^e(q,\tilde{y})$ and $\phi_{2n+2}^o(q,\tilde{y})$ are found via (2.16)–(2.22). Moreover, the orthonormality relations (2.19)–(2.20) and (2.23)–(2.24) imply that the eigenfunctions ϕ_{2n}^e and ϕ_{2n+2}^o are orthonormal. Namely, for any value of $q=2ikPe$, each eigenfunction satisfies

$$\int_0^{\pi}\phi_{2n'}^e(q,\tilde{y})\,\phi_{2n}^e(q,\tilde{y})d\tilde{y}=\frac{\pi\delta_{nn'}}{2}, \quad \text{for} \quad n,n'=0,1,2\cdots. \tag{2.28}$$

Similarly, the odd eigenfunctions satisfy

$$\int_0^{\pi}\phi_{2n'+2}^o(q,\tilde{y})\,\phi_{2n+2}^o(q,\tilde{y})d\tilde{y}=\frac{\pi\delta_{nn'}}{2}, \quad \text{for} \quad n,n'=0,1,2\cdots. \tag{2.29}$$

Lastly, using (2.16) and (2.22) and the orthogonality of normal modes, we get the following transformation (i.e., a change in basis)

$$\sum_{n=0}^{\infty}(1+\delta_{r0})A_{2r}^{(2n)}(q)\phi_{2n}^e(\tilde{y},q)=\cos{(2r\tilde{y})}, \quad r=0,1,2,\cdots, \tag{2.30}$$

and

$$\sum_{n=0}^{\infty}B_{2r+2}^{(2n+2)}(q)\phi_{2n+2}^o(\tilde{y},q)=\sin{[(2r+2)\tilde{y}]}, \quad r=0,1,2,\cdots. \tag{2.31}$$

The derivations above imply that the non-self-adjoint nature of the advection-diffusion operator (2.2) is captured by the properties of the matrices (2.21) and (2.27), determined by their dependence on $q=2ikPe$, and by the shear (through $\alpha_m\neq 0, m=1,2,\cdots$). As q is imaginary, the matrices are Hermitian only in the absence of shear ($\alpha_m\equiv 0$ for all

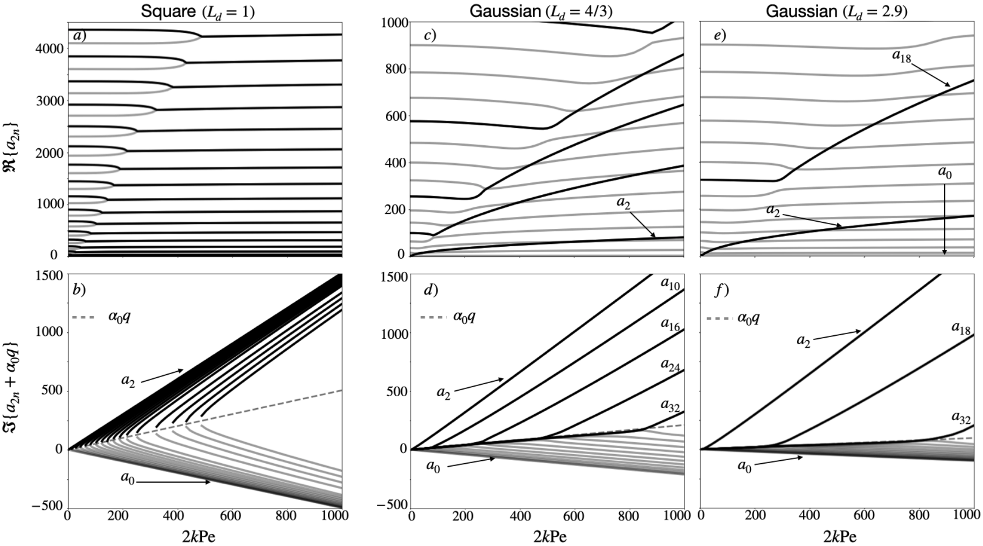

FIGURE 3. Real (top row) and imaginary (bottom row) shifted eigenvalues $a_{2n} + \alpha_0 q$ associated with the Square (a–b) and Gaussian (c–f) shear flows of different widths (see Fig. 2c). Light gray lines correspond to eigenvalues with negative imaginary parts ($\Im\{a_{2n}\} < 0$), so the shifted imaginary values lie below the dashed gray line $\alpha_0 q$. Black lines correspond to eigenvalues with positive imaginary parts ($\Im\{a_{2n}\} > 0$). In the limit $kPe \to 0$, all eigenvalues converge to $a_{2n} \to 4n^2$, $n = 0, 1, 2 \cdots$. Only the gravest 40 eigenvalues are plotted.

$m = 1, 2, 3 \cdots$), or when $q \equiv 0$ ($k = 0$ or $Pe = 0$). In those cases, the advection-diffusion operator is self-adjoint.

In the presence of shear the bi-infinite matrices $\mathbf{T}^e$ and $\mathbf{T}^o$ belong to a wide class of non-self-adjoint operators associated with $\mathcal{PT}-$symmetric Hamiltonians (Bender & Boettcher 1998; Bender 1999; Heiss 2004, 2012). A characteristic of these systems, beyond their dependence on a single parameter (here q), is the *analytical coalescing* of eigenvalues in their real parts at isolated, discrete values of the parameter $q = q_{EP}$ called *Exceptional Points* (EPs). At EPs the imaginary parts of the eigenvalues branch, to create complex-conjugate eigenvalue pairs for $q > q_{EP}$ (Hunter & Guerrieri 1981; Hernández & Mondragón 1994; Heiss 1999, 2004; Miri & Alu 2019). EPs are anticipated for all the eigenvalues for shear flows that are shift-reflect symmetric. The reason is in such flows the diagonal elements of $\mathbf{T}^e$ and $\mathbf{T}^o$ are real, and so their eigenvalues are either real or occur in complex-conjugate pairs (see Fig. 3a–b).

At EPs, the eigenfunctions coalesce too, resulting in a gap in the completeness of the set of eigenfunctions. This implies the need to supplement the set of eigenfunctions (Brimacombe *et al.* 2021). Because EPs are isolated discrete points †, however, it is extremely rare to match an EP exactly with a generic combination of k and Pe. In the rare case of an exact match, perturbing k or Pe avoids evaluating at the EP location in q-space. In practice, the ability to compute the eigenvalue spectra *a priori* allows for the inspection for EPs. If they occur, then appropriate changes to k or Pe can be made. Hence, there is no practical need to supplement the set of eigenfunctions and, for the rest of paper, we avoid explicit evaluation at EPs when computing analytical solutions.

Changing the periodicity of the shear flow by increasing the value of P (e.g., from $P = 1$

---

† e.g., the 1st EP in Mathieu's equation is $q_{EP} = 1.468768613785142i$, per Brimacombe *et al.* 2021

to $P = 2$ as seen in Fig. 2a, e) introduces multiple extrema in the shear flow profile that are shifted by $2\pi/P$ in y. If the shear flow was previously shift-reflect symmetric, the EPs of the resulting P-periodic shear flows can involve multiple eigenvalues and mergers that are more complex than the coalescence of a complex-conjugate pair.

The non-self-adjoint character of the linear operator (2.2) imprints on the spatial (via eigenfunctions) and temporal (via eigenvalues) behavior of solutions. To illustrate this point, we focus on the pair $\{a_{2n}, \phi^e_{2n}\}$ associated with shear flows that are shift-reflect symmetric; such flows represent a special case in which eigenvalues are dense with EPs. When evaluated at $q-$values beyond an EP, the eigenfunctions $\{\phi^e_{2n}\}$ associated with complex conjugated eigenvalues that have coalesced satisfy their own shift-reflect symmetry (see Appendix B, also Ziener *et al.* 2012). That is, the two symmetric eigenfunctions describe identical spatial behavior in the solution that is shifted from one another in space by $\tilde{y} = \pi/2$ ($y = \pi$). Given that the complex-conjugate eigenvalue pair describe equal eigenfunction decay rates (determined by $\Re\{a_{2n}\}$) and opposite directions of eigenfunction propagation (determined by $\Im\{a_{2n}\}$), the tracer evolution in the subdomain characterized by $U^* < 0$ is an exact mirror image of the tracer evolution in the subdomain characterized by $U^* > 0$. This means, a priori knowledge of the Fourier series of a shear flow that is shift-reflect symmetric provides a deep fundamental understanding of a global property of the tracer distribution at all times.

The present method of solution relies on the convergence of the spectra of the truncated eigenvalue systems (2.17) and (2.25) with respect to the original non-truncated bi-infinite system (see Ikebe *et al.* 1996; Deconinck & Kutz 2006; Curtis & Deconinck 2010). The convergent truncation implies there is a large enough matrix size $(R+1) \times (R+1)$ for which the eigenvalue-eigenfunction pairs calculated are sufficiently accurate. It also implies that higher cross-stream modes (in y) can be approximated by

$$a_{2n'} \approx (2n')^2, \qquad \phi^e_{2n'} \approx \cos{(2n'\tilde{y})}, \qquad n' > R+1, \tag{2.32}$$

and

$$b_{2n'+2} = (2n'+2)^2, \qquad \phi^o_{2n'+2} = \sin{[(2n'+2)\tilde{y}]}, \qquad n' > R. \tag{2.33}$$

Following Ziener *et al.* (2012), an accurate truncation is one that ensures the orthogonality relations (2.20)–(2.24) are satisfied. A first order guess for a truncated size R comes from ensuring that the truncated matrix is always diagonally dominant. Given that the diagonal term is $4R^2 \pm q\alpha_{2R}$, and $|\alpha_{2R}| \to 0$ for increasing R, a truncation size can be estimated from the ratio between the diagonal terms and the super-diagonal terms. This is†

$$4R^2 \gg |q \max\{\alpha_m\}|. \tag{2.34}$$

Since the truncated matrix size R depends explicitly on Pe via $|q| = 2kPe$, the truncated matrices $\mathbf{T}^e(q)$ and $\mathbf{T}^o(q)$ grow in size like $Pe^{1/2}$. For this reason, the present eigenvalue approach to solve the governing equation (2.2) is most efficient at intermediate and low Pe values (i.e. $Pe < 10^4$), although there is no restriction on how large Pe can be.

The value of R further quantifies the cross-stream cutoff wavenumber l_c, past which small scales become only weakly influenced by the presence of shear, and higher modes in an arbitrary initial condition decay as pure diffusion. From (2.34) we define this scale as

$$l_c = G\sqrt{|\alpha_{max}|kPe/2}, \tag{2.35}$$

† This condition implies absolute and uniform convergence of the trigonometric series 2.16 (Arscott 2014).

where $G \gg 1$ is an arbitrary constant.[‡]

The approximations (2.32)–(2.33) expose the *multiscale nature* of scalar mixing in the cross-stream direction, i.e., they reflect a pure diffusive behavior at high enough cross-stream wavenumbers for every streamwise (Fourier mode) k. In this sense, the cross-stream scale l_c complements the estimate of streamwise scale at which variance decays diffusively in the cosine shear flow (Camassa *et al.* 2010).

2.3. *General solution*

Considering only a single term in the initial condition in (2.5), and where each of $f(x)$ and $\Phi(2\tilde{y})$ is integrable such that they have Fourier series

$$f(x) = \sum_{j=0}^{\infty} c_j \cos\left(jk_m x\right), \tag{2.36}$$

and

$$\Phi(2\tilde{y}) = \sum_{l=0}^{\infty} \chi_l^e \cos\left(2l\tilde{y}\right) + \chi_l^o \sin\left(2l\tilde{y}\right), \tag{2.37}$$

where c_j, χ_l^e and χ_l^o are coefficients determined by inversion formulas from known $f(x)$ and $\Phi(2\tilde{y})$, with $j, l = 0, 1, 2, \cdots$. Using (2.30)–(2.31), we write the cross-stream initial condition (2.37) in terms of the new eigenbasis as

$$\Phi(2\tilde{y}) = \sum_{n,l=0}^{\infty} \chi_l^* A_{2l}^{(2n)}(q)\phi_{2n}^e(\tilde{y}, q) + \chi_l^o B_{2l+2}^{(2n+2)} \phi_{2n+2}^o, \tag{2.38}$$

where $\chi_l^* = (1 + \delta_{l0})\chi_l^e$. Then, the general solution to (2.2) associated with an initial condition (2.5) and doubly-periodic boundary conditions is given by the triple sum

$$\begin{aligned}\theta(x, \tilde{y}, t) = \Re\Bigg\{ \sum_{j,n,l=0}^{\infty} c_j & \left[\chi_l^* A_{2l}^{(2n)} \phi_{2n}^e \exp\left(-\frac{a_{2n}}{4}t\right) + \chi_l^o B_{2l+2}^{(2n+2)} \phi_{2n+2}^o \exp\left(-\frac{b_{2n+2}}{4}t\right)\right] \\ & \times \exp\left[ijk_m\left(x - \frac{\alpha_0 Pe}{2}t\right) - \left((jk_m)^2\right)t\right]\Bigg\}.\end{aligned} \tag{2.39}$$

The analytical solution (2.39) results from a constant U_0 and thus single Pe value. In the case of a time-varying amplitude, additional $N-$ different U_0 values that approximate $U_0(t)$ then generate $N-$ sets of eigenfunction-eigenvalue pairs, each with a solution expression that looks like that in (2.39). The ability to solve for arbitrary initial conditions via their Fourier coefficients (2.36–2.37) allows (2.39) to represent the solution to a time amplitude varying shear flow during a time-interval at which a U_0 is effectively constant.

3. Results

We now apply these new method of solution to explore the tracer evolution of two types of initial conditions: 1) A single streamwise Fourier mode (as in Fig. 1a), for which we characterize the modal decay rate, and relate it to the gravest eigenvalues, confirming and extending the asymptotic analysis of Camassa *et al.* (2010). 2) A localized concentration (tracer patch; as in Fig. 1b), for which we characterize the tracer dispersion via its central moments, extending the particle study of the Poiseuille flow by Latini & Bernoff (2001). Appendix C contains a useful reference to variable names in tabular form and in appendix

---

[‡] A value in the range $G^2 \geqslant 50$ already yields good results.

D), we provide a comparison of the analytic solutions to numerical solutions from the open source package Oceananigans (Ramadhan *et al.* 2020), with excellent results.

3.1. *Modal solutions*

3.1.1. *Localized cross-shear initial condition*

Consider a centered initial condition describing a single streamwise Fourier mode that is localized in the cross-stream direction:

$$\theta(t=0) = \cos(kx)\exp\left[-4(y-\pi)^2\right]. \tag{3.1}$$

The analytical solution with this initial condition is (2.39) for a single mode k and cross-stream coefficients

$$\chi_l^* = \frac{1}{2\sqrt{\pi}}\exp(-il\pi)\exp\left[-\left(\frac{l}{4}\right)^2\right], \quad l = 0, 1, 2\cdots . \tag{3.2}$$

The $l = 0$ term implies the presence of a non-zero cross-stream average, although the global (area average) remains zero. We refer to the initial condition (3.1) as *modal* and *centered*, given the absence of odd cross-stream Fourier coefficients ($\chi_l^o \equiv 0$ in (2.38)).

Snapshots of solutions θ to (2.2) for a Gaussian shear flow ($L_d = 4/3$) are shown in Fig. 4. At low $q = 4i$ (Fig. 4a–d), the long term evolution of θ settles into a domain-scale structure. The solution does not clearly exhibit the two distinct spatially-separated behaviors associated with subdomains defined by our choice of $U^* < 0$ and $U^* > 0$. At larger $q = 640i$, the solution does exhibit two distinct behaviors (Fig. 4e–h). Given our choice of flow normalization, tracer variance is homogenized much more rapidly near the peak of the shear flow ($U^* > 0$) than away from it ($U^* < 0$)†. The initial condition centered at $y_0 = \pi$ facilitates the distinction between the subdomains $U^* > 0$ and $U^* < 0$ for large enough q although an arbitrary initial condition may not. Such behavior is associated with the localization of the eigenfunctions within shear free-regions as q becomes large.

To quantify the transient and long-term decay of tracer variance, we compute

$$\sigma = -\frac{1}{2}\frac{d\log\left(\|\theta\|_2^2\right)}{dt}, \tag{3.3}$$

where $\|\theta\|_2^2$ is the L_2-norm defined by

$$\|\theta\|_2^2(t) = \int_{-\pi/k}^{\pi/k}\int_0^{2\pi} \theta^2\, dy\, dx. \tag{3.4}$$

With initial condition (3.1), we identify two non-overlapping plateaus in the σ time series for sufficiently small streamwise scales, or equivalently sufficiently large Pe. Each plateau implies that a single eigenvalue-eigenfunction dominates the (spatio-temporal) decay rate of tracer variance, with tracer localized to regions where U^* has an extrema (see Fig. 5a–d). We refer to the plateaus as *pure modal decay rates* denoted as $\overline{\sigma}$. Varying k at constant Pe reveals the $q-$dependence of the gravest two eigenvalues, as seen in Fig. 5e. These are the (averaged) modal decay rates estimated in Camassa *et al.* 2010 in that case for the cosine shear flow. An off-centered initial condition ($\chi_l^o \neq 0$) can yield a σ time series in which the two plateaus overlap, and distinguishing between the two even eigenvalue-eigenfunction pairs can be unclear.

---

† The actual sign of U^*, which arises from our particular choice of mean velocity, has no direct effect on the decay rate of tracer variance.

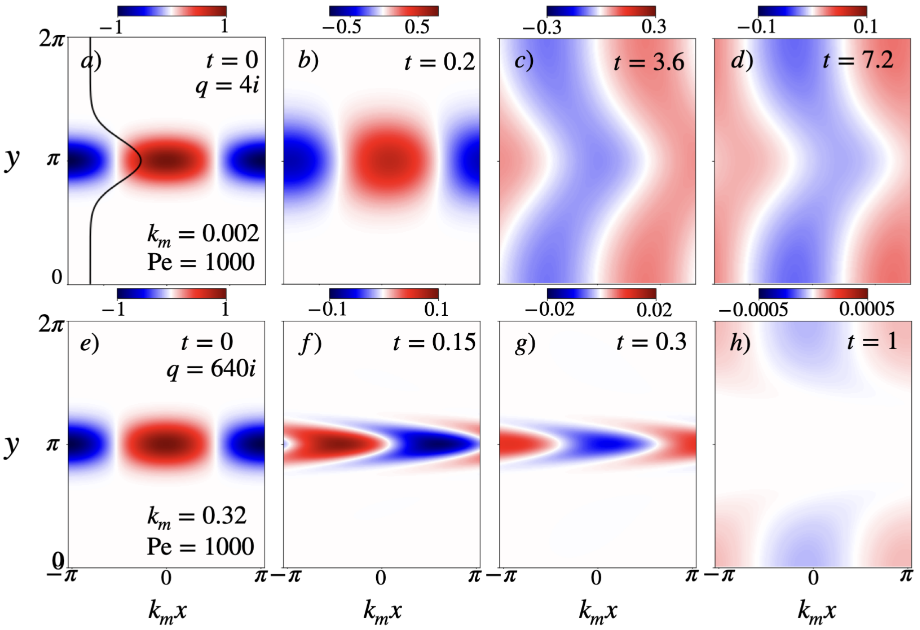

FIGURE 4. Snapshots of modal solutions for two wavenumbers k_m and two values of canonical parameter $q = 2ik_m Pe$ at fixed $Pe = 1000$. The shear flow is Gaussian with inverse width parameter $L_d = 4/3$ (black curve in panel (a) and Fig. 2c). The streamwise axis is scaled by (domain-scale) wavenumber k_m, and the colorscales differ between panels.

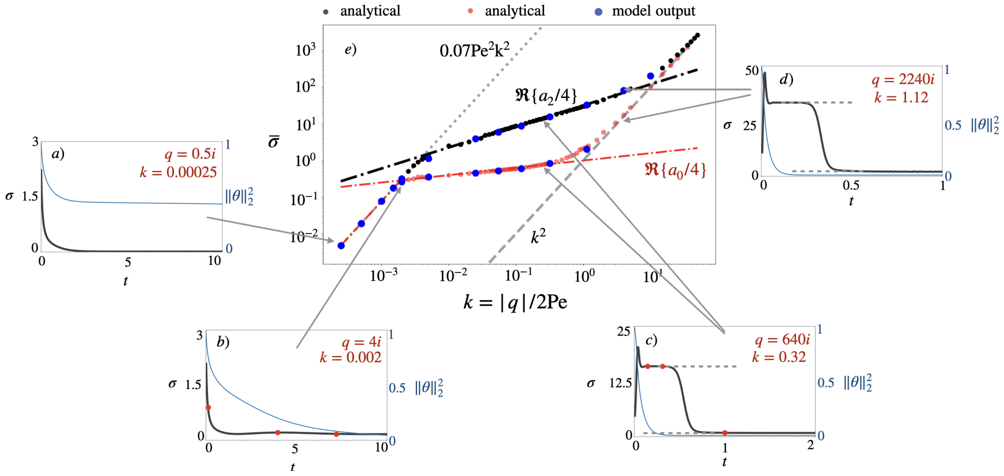

FIGURE 5. a)–d) Time series of decay rate $\sigma(t)$ (black) and variance $\|\theta\|_2^2$ (blue, normalized by its initial value) for fixed $Pe = 1000$ and various choices of wavenumber k (hence canonical parameter $q = 2ikPe$) in the modal initial condition (3.1). The shear flow is Gaussian ($L_d = 4/3$). The red dots in b) and c) represent the times of the snapshots shown in Figs. 4a–d and e–h, respectively. e) Pure modal decay rate $\overline{\sigma}$ (see text) showing the distinct regimes of scalar decay as a function of streamwise wavenumber k. The black and red dots are from analytical solutions and blue dots are from numerical simulations. Shown in e) are the asymptotic curves for the gravest eigenvalues a_2 (black, at large q) and a_0 (red, at both small and large q). Grey arrows connect the distinct σ time series in panels a)–d) with their averaged values in panel e). Note that the log-log plot accentuates large and small k behavior.

Shear flow	P	$\lvert q_{cr}\rvert$
Cosine		
$\alpha_1 = 0.25$	1	3.0455
Triangular		
$L_d = 1/2$	1	3.6805
$L_d = 1/2$	2	14.9002
$L_d = 1/2$	3	32.1463
$L_d = 1$	1	0.5506
$L_d = 2$	1	0.821
Square		
$L_d = 1$	1	2.3643
$L_d = 1$	2	9.2947
$L_d = 1$	3	20.298
$L_d = 2$	1	0.4204
$L_d = 5.2$	1	0.7612
Gaussian		
$L_d = 4/5$	1	0.6503
$L_d = 4/3$	1	0.5506
$L_d = 2.9$	1	0.821
Polynomial		
$L_d = 1$	1	0.7043
$L_d = 2$	1	0.65035
$L_d = 3$	1	0.7612
$L_d = 5$	1	0.9496

TABLE 1. Critical canonical parameters $|q_{cr}|$ for shear flows considered. The parameter P represents the periodicity of the shear flow within the domain. $P = 1$ in a single peaked (single maxima), $P = 2$ and $P = 3$ imply two and three shear flow maxima (peaks), respectively, as shown in Figs. 2e–h.

Figure 6 shows that the three regimes of scalar decay, described by Camassa *et al.* (2010) for the cosine shear flow, are present in all shear flows, and are therefore generic. For arbitrary Pe, we define these three regimes using a critical canonical parameter q_{cr} as follows: For small q values, $|q| < |q_{cr}|$, the gravest eigenvalue is real (see Table 1). Thus, at long-enough (streamwise) scales $k < O(1)$, $|q| < q_{cr}$, and $\overline{\sigma} \propto k^2$, with a coefficient proportional to Pe^2. This is the regime of Taylor dispersion because it describes a diffusion process with effective diffusivity κ^*, given dimensionally by

$$\kappa^* = \frac{U_0^2 M^2}{2\pi^2 \kappa} \sum_{m=1}^{\infty} \frac{\alpha_m^2}{2m^2}. \tag{3.5}$$

The exact result $\beta_2 = \sum_{m=1}^{\infty}(\alpha_m^2/(2m^2))$ is derived in Appendix E, for all shear flows considered here. This expression for the effective diffusivity matches that first derived in Zel'dovich (1982) for time-oscillatory, periodic shear flows (when considering vanishing frequency; see also Majda & Kramer 1999; Smith 2005; Haynes & Vanneste 2014).

At intermediate scales, $k > |q_{cr}|/(2Pe)$, the gravest eigenvalue a_0 becomes complex and the pure modal decay rate is *anomalous*, meaning $\overline{\sigma} \propto k^s$ with $s < 2$. In fact, pure modal decay rates in the $U^* > 0$ and $U^* < 0$ regions generally separate (see Fig. 6). Only when the flow is shift-reflect symmetric, like in the cosine, triangular and square shear flows, where eigenvalues appear as complex conjugated pairs, do we find a single pure modal decay rate to determine the anomalous modal decay for all values of q.

The algebraic dependence of the gravest eigenvalues at large q can be derived via a WKB analysis localized to regions with vanishing shear where U^* has an extrema. In other words, the values of $\overline{\sigma}$ in this asymptotic limit explicitly depend on the gradient of shear at the flow extrema, where shear changes sign (e.g., see Hunter & Guerrieri 1981;

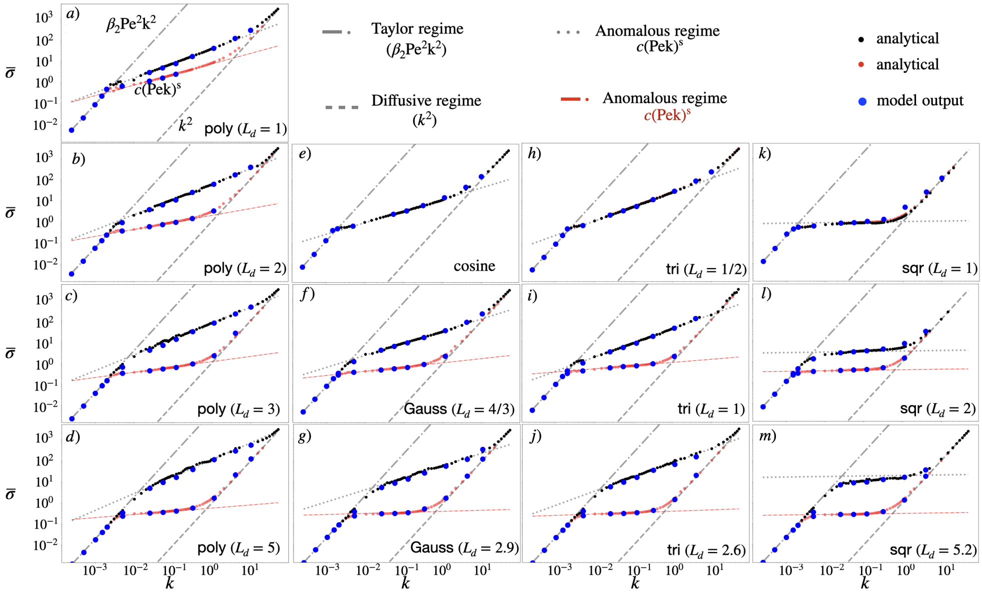

FIGURE 6. Pure modal decay rate $\bar{\sigma}$ for all flows considered with single maxima ($P = 1$). The different lines are from analytical predictions of the asymptotic behavior of the gravest eigenvalues a_0 and a_2 at large and small q, along with the pure diffusion case k^2. In all cases, $Pe = 1000$. For values of the β_2, c and s coefficients, see Table 2.

shear flow	$a_0/4 \sim \beta_2 Pe^2 k^2$	$\Re\{a_{2n}^-/4\} \sim c_-(kPe)^{s-}$		$\Re\{a_{2n}^+/4\} \sim c_+(kPe)^{s+}$	
	β_2	s_-	c_-	s_+	c_+
Cosine					
$\alpha_1 = 0.5$	0.125	0.5	0.27	0.5	0.27
Triangular					
$L_d = 1/2$	0.0822	0.67	0.258	0.67	0.258
$L_d = 1$	0.0874	0.05	0.6	0.67	0.377
$L_d = 2.6$	0.0228	0.025	0.3	0.67	0.71
Square					
$L_d = 1$	0.2056	0.025	0.83	0.025	0.83
$L_d = 2$	0.1156	0.025	0.35	0.025	2.71
$L_d = 5.2$	0.02484	0.025	0.266	0.025	16.82
Gaussian					
$L_d = 4/5$	0.1166	0.48	0.26	0.5	0.48
$L_d = 4/3$	0.0757	0.18	0.27	0.5	0.97
$L_d = 2.9$	0.02351	0.065	0.26	0.5	2.12
Polynomial					
$L_d = 1$	0.08355	0.5	0.23	0.67	0.38
$L_d = 2$	0.05528	0.33	0.2	0.7	0.45
$L_d = 3$	0.0364	0.25	0.2	0.7	0.58
$L_d = 5$	0.01868	0.167	0.19	0.7	0.79

TABLE 2. Parameters that determine the pure modal decay rates $\bar{\sigma}$ in Taylor's and the anomalous diffusion regimes of shear dispersion. To visualize these values, see Fig. 6.

Camassa *et al.* 2010). The eigenvalues take the form

$$a_{2n} \sim d_1 q^s - d_2 q, \tag{3.6}$$

where d_1 and d_2 are coefficients independent of q, and the exponent $s < 2$ is real. But the asymptotic behavior (3.6) only strictly applies in the limit of $|q| \to \infty$ where the

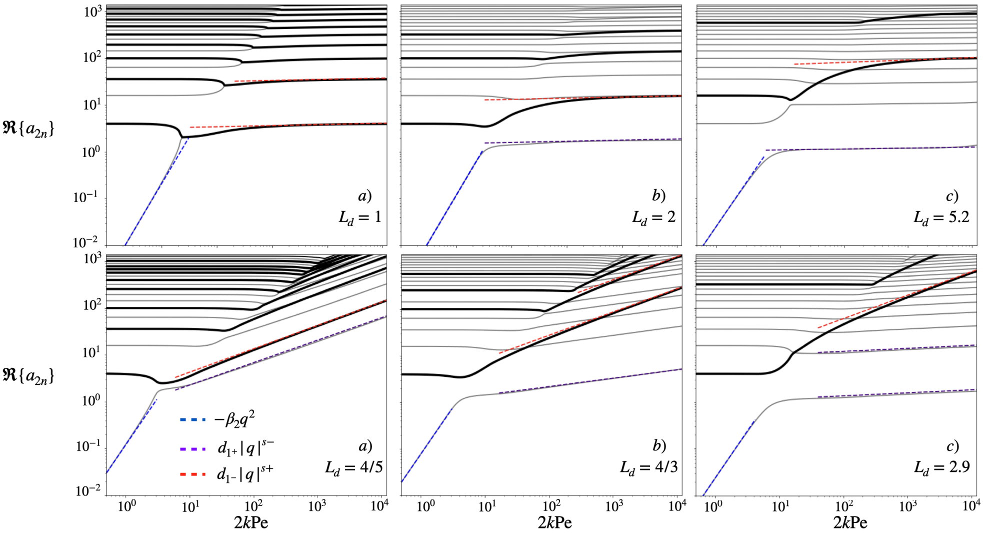

FIGURE 7. Fits (dashed lines) to the gravest eigenvalues with positive (thick black curves) and negative (thin gray curves) imaginary parts for a)–c) square and d)–f) Gaussian shear flows for various inverse width parameters L_d (see Fig. 2).

eigenfunctions are localized to shear-vanishing regions and remains greatly inaccurate at intermediate q values near q_{cr} (the actual range of validity varies for each shear flow). This severely constrains the applicability of asymptotic (pure) modal decay rates to realistic flows with finite Pe values, and arbitrary initial conditions† Fig. 7a–c shows this error for the square shear flow in the estimate of pure modal decay rates (red dash lines) as these get extrapolated towards intermediate $q-$values near q_{cr}. The implication is that for arbitrary Pe values, the asymptotic approach incorrectly predicts faster (pure modal) decay rates of tracer variance, meaning an over-mixing at intermediate scales.

Given that the asymptotic expression (3.6) provides an accurate approximation of $\overline{\sigma}$ at large k, and we use it following Camassa *et al.* (2010) to estimate the streamwise scale of transition into the pure diffusion regime, for the long-lived tracer patches localized within shear vanishing regions. This represents the (streamwise) scale at which decay of tracer variance of the longest-lived tracer patches becomes insensitive to cross-stream shear. Excluding shift-reflect symmetric flows, two distinct $\overline{\sigma}(k)$ curves exist, and so this transition varies across the domain.

At large q values, the pure modal decay rate takes the form

$$\overline{\sigma}^{\pm} \sim c_{\pm}\,(kPe)^{s_{\pm}}\,, \tag{3.7}$$

where the ± signs reflect the positive (+) and negative (−) signs of the imaginary parts of the eigenvalues (and hence the sign of U^{*}). From (3.6), the coefficients connect as

$$c_{\pm} = \frac{2^{s_{\pm}}\,d_{1\pm}}{4}. \tag{3.8}$$

From the fitted coefficients $s_{\pm}$ and $d_{1\pm}$ and (3.8) we calculate $c_{\pm}$ and list them in Table

---

† It is successfully applied in (Camassa *et al.* 2010) to describe the evolution of a multiscale initial condition which concentrates tracer variance at very large scales and very small scales, well separated in spectral space.

2. Using (3.7), the transition scale k_d into the pure diffusion regime is

$$k_d^{\pm} = \left(c_{\pm} Pe^{s_{\pm}}\right)^{\frac{1}{2-s_{\pm}}} . \tag{3.9}$$

For values of $s^{+} = 0.5$ typical for the Gaussian shear flows, $k_d \propto Pe^{1/3}$, equating that of the cosine shear flow previously derived (see Camassa *et al.* 2010). From (3.9) we find a strong dependence of the Pe scaling the type of shear (e.g., piecewise linear, continuous, constant) from the computed values of $s_{\pm}$ parameter, and therefore a spatial dependence of the Pe scaling when flows are not shift-reflect symmetric. This means that the decay rate of tracer variance decays as pure streamwise diffusion over two distinct range of modes, if the shear curvature is different in the different shear-vanishing regions. This can be seen clearly in the narrow flows in Fig. 6k–m, for which there are two distinct range of (streamwise) scales which decay diffusively.

Moreover, since (3.9) relies on the accuracy of (3.6), such transition scale is only accurate under the large q limit. In our eigenfunction-approach, the transition scale for arbitrary Pe values can be computed directly form the eigenvalues a_0 and a_2 calculated from matrices $\mathbf{X}^e$ and $\mathbf{X}^o$, but the functional dependence on Pe as expressed in (3.6) is not easily available given the unknown analytical expression $a_{2n} = a_{an}(q)$ at intermediate $q-$values.

The intermediate q values are also significant in the case of time-varying amplitude, given that varying Pe which is equivalent to varying the amplitude of the shear flow. In that case, the curves $\beta_2 Pe^2 k^2$ in Fig. 6 associated with the small q limit (Taylor's regime of scalar decay) and those of the anomalous decay shift vertically, although former regime is much more sensitive to time-amplitude changes due to the Pe^2 dependence. The pure diffusion (k^2) remains insensitive to Pe values, but what sensitive is, as mentioned in the previous paragraph, the scale of transition $k_d^{\pm}$ into the pure diffusion regime.

From all the values of $s_{\pm}$ in Table 2, observe that:

(i) When shear is discontinuous (like in the polynomial and triangular shear flows) $s_{+} \approx 2/3$, independent of the width of the flow L_d.

(ii) When shear is continuous, the exponent lies in the range $0.025 \leqslant s \leqslant 0.5$, and the largest exponent is associated with flows whose local curvature is quadratic. The smallest exponent corresponds to the square shear flow. These results are independent of the width of the flow L_d.

The observations (i)–(ii) were first shown for the cosine and linear shear flow (Camassa *et al.* 2010), and we show that these are universal across any shear flows that has an integrable dependence on y, independent of shear flow width. However, as the shear flows narrow (L_d increases), increasingly large values of $|q|$ are necessary for the eigenvalues to asymptote, according to (3.6). This behaviour leaves an increasingly large range of intermediate q values (hence scales k for arbitrary Pe) for which (3.6) is inaccurate, most obviously for the square shear flow (solid black and dashed red lines in Fig. 7a–c). This implies an over-mixing estimate within regions of vanishing shear, and under mixing away from these regions, at intermediate scales. For time- amplitude varying shear flows that continuously reassign Fourier modes onto new q values†, such spurious mixing behavior would only be accentuated.

---

† Any change to the amplitude of a shear flow is equivalent to modifying the Pe value in our analysis.

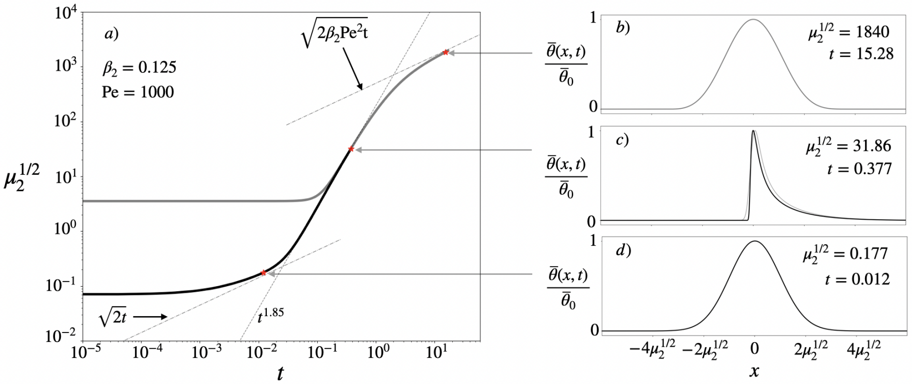

FIGURE 8. a) Time evolution of the streamwise tracer width $\mu_2^{1/2}$ in two domains and for two initial widths: $\mu_2^{1/2}(0) = 5/4$ shown in gray and computed using a wider domain (see text), and $\mu_2^{1/2}(0) = 1/20$, shown in black and computed using a smaller domain. b–d) Snapshots of the averaged, normalized plume, corresponding to a different stage of the dispersion process. In c), we superimpose the two concentrations with equal width associated with different initial conditions and domain lengths. In both cases, $y_0 = 0$, $U(y) = 1/2(1 - \cos(y))$ and cross-stream width is 1/100.

3.2. *Time varying dispersion of a localized concentration*

We now consider the time-varying dispersion of a tracer patch defined by the initial condition

$$\theta(x, y, 0) = \exp\left[-\left(\frac{x}{\sqrt{2\mu_2(0)}}\right)^2 - \left(\frac{y - y_0}{\sqrt{0.02}}\right)^2\right]. \tag{3.10}$$

The initial widths of the patch in the cross- and stream- wise directions are 1/100 and $\mu_2^{1/2}(0)$, respectively.† A large literature exists on the time evolution of a localized plume in laminar flows, and the enhanced transport that derives from the combined action of differential advection and mixing (i.e. shear dispersion; see Aris 1956; Elrick 1962; Lighthill 1966; Young *et al.* 1982; Rhines & Young 1983; Latini & Bernoff 2001; Ferrari *et al.* 2001; Haynes & Vanneste 2014). The goal here is to characterize the distinct stages of shear dispersion, highlighting the self-similar processes.

We investigate the streamwise dispersion by tracking the time-evolution of the second moment of the cross-stream-averaged concentration $\overline{\theta}$. As the flow is unidirectional, we only consider the central moments of the streamwise direction. The pth-moment is defined as

$$\mu_p = \int_{-\infty}^{\infty} |x - \mu|^p \left(\overline{\theta}/\overline{\theta}_0\right) dx, \tag{3.11}$$

where $\overline{\theta}_0 = \overline{\theta}(t = 0)$ and

$$\mu = \int_{\infty}^{\infty} x(\overline{\theta}/\overline{\theta}_0) dx. \tag{3.12}$$

Our definition 3.11 ensured then that $\mu_0 = 1$ and $\mu_1 = 0$. When characterizing the dispersion process, we are interested in the limit in which the pth-moment achieves the

---

† We define the initial streamwise width using the nomenclature associated with the 2nd central moment in (3.11) at time $t = 0$.

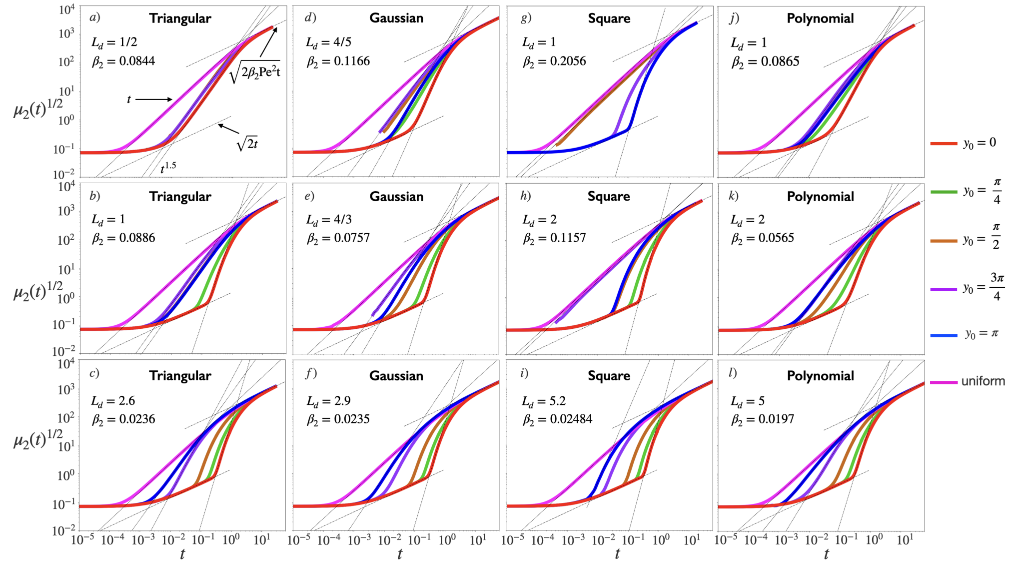

FIGURE 9. Stages of the dispersion process as a function of time. Each curve represents the evolution of the width of an initially-localized tracer patch, with the width defined as the square root of the second moment μ_2 via (3.11). Each colored line is associated with a different choice of y_0 (see the labels on the right). Also shown are two diffusive curves proportional to $t^{1/2}$, and several super-diffusive power-laws (gray lines). The magenta line is for an initial condition that is uniform in the across-stream direction. In all cases, $Pe = 1000$.

(self-similar) power law

$$\mu_p \sim |t|^{\gamma_p}. \tag{3.13}$$

Dispersion processes are characterized by γ_2 in the following manner: The process is diffusive when $\gamma_2 = 1$, is sub-diffusive when $\gamma_2 < 1$, and is super-diffusive when $\gamma_2 > 1$. A dispersion process that is not diffusive ($\gamma_2 \neq 1$) is called an anomalous-diffusion process (Weeks *et al.* 1996; Castiglione *et al.* 1999; Ferrari *et al.* 2001).

Consider the case of $Pe = 1000$ value and a streamwise domain length $-5000\pi \leqslant x \leqslant 5000\pi$, hence $k_m = 2/5000$. This choice of domain size ensures that the gravest modes capture the Taylor diffusion regime of scalar decay ($\overline{\sigma} = \beta_2 Pe^2 k^2$), for our choice of Pe value. We also are interest in a narrow initial width, $\mu_2^{1/2}(0) \sim O(10^{-1})$, so that the initial condition incorporates sufficiently large wavenumbers within the regime of pure diffusive decay ($\overline{\sigma} = k^2$). For each streamwise wavenumber k that arises from the discretization of the domain we need to solve a non-Hermitian eigenvalue system (described in §2.2). The task of solving for a localized plume in a extremely long domain can become computationally expensive.

To facilitate the computation of solutions, we exploit the self-similar time-evolution of $\overline{\theta}(x,t)$ (see Fig. 8) and consider two different domain lengths to evaluate different initial widths: For a narrow initial width, $\mu_2^{1/2}(0) = 1/20$, we consider the smaller domain $100\pi \leqslant x \leqslant 100\pi$, discretized spatially by $N_x = 60001$. For a larger initial width, $\mu_2^{1/2}(0) = 5/4$, we consider the larger domain $-5000\pi \leqslant x \leqslant 5000\pi$, discretized by $N_x = 30001$ points. We then compute the full time evolution of $\mu_2^{1/2}(t)$ from a composite of the two initial conditions considered, as shown for the cosine shear flow in Fig. 8.

In all steady, laminar parallel shear flows explored, we find that the solution evolves through three distinct stages of dispersion (see Fig. 9), in agreement with the study

shear flow	uniform	$y_0 = 0$	$y_0 = \pi/4$	$y_0 = \pi/2$	$y_0 = 3\pi/4$	$y_0 = \pi$
cosine	$(350, 1)$	$(200, 1.875)$	$(250, 1.45)$	$(335, 1.45)$	$(250, 1.45)$	$(200, 1.875)$
triangular						
$L_d = 1/2$	$(300, 1)$	$(135, 1.5)$	$(245, 1.475)$	$(245, 1.475)$	$(245, 1.475)$	$(135, 1.5)$
$L_d = 1$	$(325, 1)$	$(175, 3.2)$	$(375, 2.6)$	$(300, 1.5)$	$(480, 1.475)$	$(280, 1.5)$
$L_d = 2$	$(235, 1)$	$(60, 3.6)$	$(160, 3.2)$	$(750, 2.85)$	$(1900, 2)$	$(660, 1.475)$
square						
$L_d = 1$	$(350, 1)$	$(1600, 3.6)$	$(7000, 3)$	$(325, 1)$	$(7000, 3)$	$(1600, 3.6)$
$L_d = 2$	$(350, 1)$	$(220, 3.95)$	$(735, 3.4)$	$(6000, 3)$	$(375, 0.975)$	$(10000, 3)$
$L_d = 5.2$	$(250, 0.975)$	$(75, 4)$	$(300, 3.8)$	$(1800, 3.325)$	$(7800, 2.5)$	$(25000, 2.35)$
Gaussian						
$L_d = 4/5$	$(350, 1)$	$(145, 2.4)$	$(190, 1.75)$	$(350, 1.5)$	$(450, 1.45)$	$(370, 1.8)$
$L_d = 4/3$	$(325, 1)$	$(150, 3.6)$	$(280, 2.8)$	$(500, 2)$	$(625, 1.45)$	$(700, 1.75)$
$L_d = 2.9$	$(210, 0.975)$	$(60, 3.6)$	$(160, 3.2)$	$(1000, 3)$	$(1700, 2)$	$(1500, 1.65)$
polynomial						
$L_d = 1$	$(295, 1)$	$(115, 1.97)$	$(150, 1.55)$	$(262, 1.5)$	$(325, 1.45)$	$(200, 1.425)$
$L_d = 2$	$(270, 1)$	$(85, 2.8)$	$(135, 2.1)$	$(240, 1.675)$	$(460, 1.5)$	$(285, 1.37)$
$L_d = 5$	$(180, 0.975)$	$(50, 3.4)$	$(105, 2.85)$	$(435, 2.55)$	$(700, 1.75)$	$(405, 1.3)$

TABLE 3. Parameter pair $(A, \gamma_2/2)$ that approximates the power law dependence of width $\sqrt{\mu_2} \approx At^{\gamma_2/2}$ (calculated empirically) in the anomalous diffusion stage. Some of these cases are shown in Fig. 9.

by Latini & Bernoff (2001) for the Poiseuille shear flow (that flow corresponds to the polynomial with $L_d = 1$ considered in this study, only shifted by π in y). These stages parallel the three regimes of scalar decay explored in the previous section, and are: an initial pure diffusion stage in which $\mu_2 = 2t$, an intermediate, anomalous (super) diffusion stage, and a final stage of enhanced diffusion $\mu_2 = 2\beta_2 Pe^2 t$ that corresponds to Taylor's dispersion (Taylor 1953; Aris 1956).

Of the three stages of shear dispersion, only the (transient) anomalous diffusion is sensitive to the choice of y_0 in the initial condition, (see Fig. 9), the exception being the *ballistic dispersion* ($\sqrt{\mu} \propto t$) associated with a uniform tracer distribution in the cross shear direction, first studied by Lighthill (see Lighthill 1966; Latini & Bernoff 2001). Table 3 summarizes the power law approximation to the width $\sqrt{\mu_2} = At^{\gamma_2/2}$ in the anomalous diffusion stage for all shear flows considered. In general, our calculated values for $\gamma_2 \approx 4$ for the polynomial shear flow ($L_d = 1$) at $y_0 = 0$, and $\gamma_2 \approx 3$ for the ($L_d = 1/2$) triangular shear flow (everywhere) coincide with previously calculated values in the literature (Elrick 1962; Rhines & Young 1983; Latini & Bernoff 2001; Meunier & Villermaux 2010, 2022)

The initial and final stages of the dispersion of an isolated tracer patch are determined by the pure diffusion and Taylor's enhanced diffusion, respectively. The characteristics of these stages are known already from $\beta_2 Pe^2$ (section §3.1) because both processes are self-similar, insensitive to y_0, and it is known that transition into Taylor's diffusion happens at $t \gtrsim O(1)$. The timescale for transition from pure diffusion into anomalous diffusion, call it τ, is calculated from the intersection of the two curves $\sqrt{2t}$ and $At^{\gamma_2/2}$. Hence, $\tau = (2/A^2)^{1/(\gamma_2-1)}$, with γ_2 and A given empirically (Table 3).

The envelope of curves $At^{\gamma_2/2}$ associated with the anomalous diffusion stage of shear dispersion in Fig. 9 shows that τ is smallest for ballistic dispersion (magenta curves in Fig. 9). Ballistic dispersion is typically associated with a uniform initial condition in the cross-shear direction, i.e. a streamwise Gaussian stripe. In this case, the initial tracer patch spans both subdomains $U^* > 0$ and $U^* < 0$, its width grows linearly with time as $\sqrt{\mu_2} \propto Pet$. We find that the constant of proportionality $\sim 0.3 \pm 0.1$ for all shear flows. Using $A = 0.3Pe$, we compute $\tau \approx 20Pe^{-2}$, or 2×10^{-5} with $Pe = 1000$. Ballistic dispersion also occurs when the initial plume with small cross-shear width is placed at a streamline with infinite shear (in the square shear flows we see it at $y_0 = \pi/2$ when $L_d = 1$, and $y_0 = 3\pi/4$ when $L_d = 2$). In both cases, $\overline{\theta}$ is composed to two asymmetric, long tailed profiles that separate from one another, as opposed to the single-tailed case in Fig. 8c.

The timescale τ of transition into the anomalous diffusion is delayed the most when the initial condition is placed in regions with zero shear over a wide range of streamlines. The square shear flow is a good example (at $y_0 = n\pi$, n an integer), in particular at $y_0 = 0$ and $L_d = 5.2$ (red curve in Fig. 9i). Taking the values of $(A, \gamma_2) = (75, 4)$ associated with the square shear flow $L_d = 5.2$ from Table 3, we find $\tau \approx 0.3$. At this timescale, the plume width transitions from growing diffusively (as $\sqrt{2t}$) to growing with a very steep anomalous diffusion (see red curves in Fig. 9c, f, i, l).

Contrary to our naive expectations, we found no direct connection between the timescale τ that indicates the transition from pure diffusion to anomalous diffusion in the evolution of the dispersion process, and the inverse scale $k_d^{\pm}$ of transition from (pure modal) anomalous tracer variance decay rate into pure diffusion decay rate ($k_d^{\pm}$). This simply implies that the eigenfunctions ϕ_{2n}^e, ϕ_{2n}^o also play an important role in determining the transition from Gaussian symmetric to asymmetric cross-flow concentrations, i.e. via a Fourier inversion (see Fig. 8c–d). Similarly, we found no connection between the values of s with the power law behavior of the γ_2, not even in the cases where the tracer was initialized at the exact streamlines where shear vanishes. That is, we found no explicit connection between the values $\gamma_2 = 2/3$ and $s = 0.75$ derived for the triangular shear flow (e.g. $L_d = 1/2$).

The anomalous diffusion stage of shear dispersion is sensitive to the choice of y_0, with implications for the self-similarity of the process. Following Castiglione *et al.* (1999); Ferrari *et al.* (2001), a process is called strongly self-similar whenever the moment's exponent γ_p is linear with p, i.e., when $\gamma_p = p/\nu$, with ν an empiric constant. Otherwise, when γ_p is piecewise linear, or nonlinear with p, the process is called weakly self-similar. An important characteristic of a strongly self-similar process (like diffusion) is that it satisfies the scaling law

$$\overline{\theta}(x,t) \approx t^{-1/\nu} \mathcal{C}\left(\frac{x}{t^{1/\nu}}\right), \tag{3.14}$$

where $\mathcal{C}$ is a scaling function (e.g., Gaussian in the case of normal diffusion) and ν is a scaling exponent ($\nu = 2$ for normal diffusion). The scaling law suggests a scaling variable $\xi = x/t^{1/\nu}$, and thus implies that the width of the tracer patch (or equivalently cloud of particles) grows as $t^{1/\nu}$(Zaburdaev *et al.* 2015). Hence, a strongly self-similar process is entirely determined by ν (the values of ν for flows discussed in the following paragraph are reported in Fig. 10a–d).

The quadratic shear flow (polynomial shear with $L_d = 1$) has a strongly self-similar, anomalous diffusion stage for various choices of y_0, but is weakly self-similar when $y_0 = \pi/4$. The value $\nu \approx 1/2$ at $y_0 = 0$ coincides with the asymptotic value derived in Latini & Bernoff (2001). A different choice of y_0, however, changes the value of ν. The triangular shear flow ($L_d = 1/2$), on the other hand, has a strongly self-similar anomalous diffusion stage that is insensitive to y_0. Specifically, $\nu \approx 2/3$ in all cases (Fig. 10e–h). The triangular shear flow with $L_d = 1$ has an anomalous diffusion stage that is strongly self-similar when the plume is initialized in regions with linear shear (Fig. 10k–l). But when the plume is initialized in regions with no shear, the anomalous diffusion exhibits weak self-similarly (Fig. 10i–j).

The scaling exponents $\nu < 2$ are typically associated with super diffusive processes

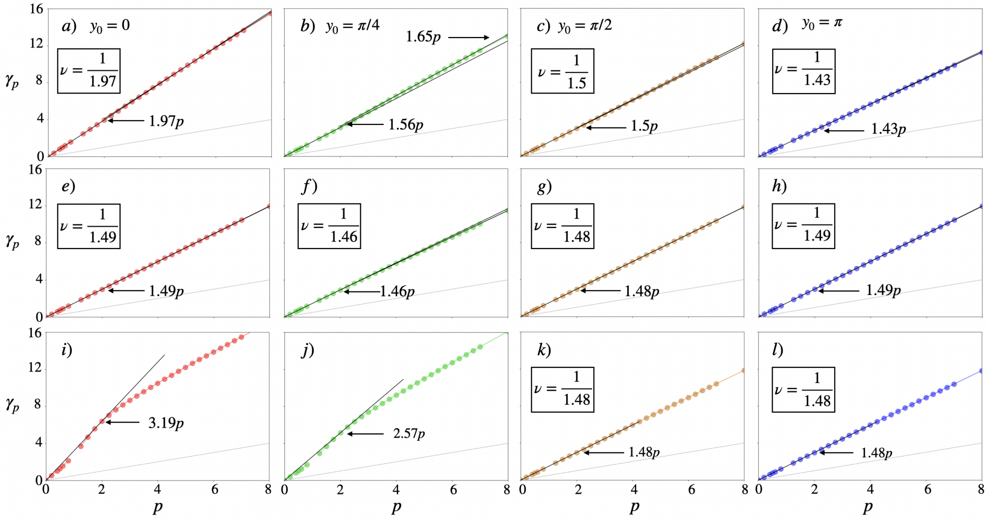

FIGURE 10. Moment γ_p dependence on moment index p for three shear flows: a)–d) Polynomial flow with $L_d = 1$ (Poiseuille-like flow, see Fig. 2d), e)–h) triangular shear flow with$L_d = 1/2$ (see Fig. 2a), and i)–l) triangular shear flow with $L_d = 1$ (also in Fig. 2a). y_0 values, fixed for each column (color coded to coincide with those in Fig. 9), are shown on top row. When $\gamma_p = p/\nu$, the value of ν is shown. Gray line shows the pure diffusive behavior $p/2$.

such as Levy walks, a stochastic that generalizes Brownian diffusion in the sense that the concentration can obey a fractional Fokker Planck equation (FFPE) (Dubkov *et al.* 2008). Previous studies have shown that weak self-similar processes fail to be represented by the scaling law (3.14) and obey neither a Fick equation nor other linear equations involving temporal and/or spatial fractional derivatives (Castiglione *et al.* 1999; Ferrari *et al.* 2001). We expand on this by showing that even flows with a strongly self-similar dispersion in its (transient) anomalous diffusion possess a non-unique exponent ν. The exception being the (wide) triangular shear flow ($L_d = 1$), which has a unique scaling exponent, insensitive to the location of the initial condition when the cross-stream width is vanishingly small.

4. Discussion

In this study, we present a new method to compute analytical solutions to the advection-diffusion equation when the advecting velocity is a steady, parallel shear flow, a building block for time-varying flows of the form (1.2). The method relies on the ability to calculate the eigenvalue-eigenvectors associated with the non-self-adjoint advection-diffusion operator (2.2), through a convergent truncation of a bi-infinite matrix constructed following a procedure similar to the Floquet-Fourier-Hill method (Deconinck & Kutz 2006). The truncated matrix, for example, implies that for every streamwise Fourier mode k in a given initial condition with an even Fourier series in the cross-stream direction ($\chi^o = 0$ in (2.39)), the solution to (2.2) is approximated via

$$\theta \approx \Re\left\{\sum_{n,l=0}^{R} \chi_l^* A_{2l}^{(2n)} \phi_{2n} \exp\left[ik\left(x - \frac{\alpha_0 Pe}{2}t\right) - \left(\frac{a_{2n}}{4} + k^2\right)t\right]\right\} + \theta_{R_>}, \tag{4.1}$$

where

$$\theta_{R_>} = \sum_{l=R+1}^{\infty} \chi_l^* \cos(ly) \cos\left[k\left(x - \frac{\alpha_0 Pe}{2} t\right)\right] \exp\left[-\left(k^2 + l^2\right) t\right]. \tag{4.2}$$

The $\theta_{R_>}$ contributions coincide with solutions to the diffusion equation, which means that the variance of tracer with cross-flow scales $l_c > R$ decays in the pure diffusion regime.

The analytical method described in §2.2 is easily expanded to handle shear flows that have a general Fourier series, as well as Neumann (tracer) boundary conditions in the cross-stream direction. Applying Neumann (no-flux) boundary conditions requires three steps, with little modification to the method: 1) Increase the periodicity of the shear flow, say from $P = 1$ to $P = 2$. 2) Restrict the analysis to only half of the domain (so that it gives the appearance of a single peaked shear flow). 3) Given an arbitrary initial condition, consider a second image initial condition, symmetric about the closest boundary $y = \pi$ or $y = 0$.

Expanding the method to handle a shear flow with arbitrary Fourier series is also straightforward, in a similar way to incorporating Neumann boundary conditions described in the previous paragraph. Again, there are three steps: Given an arbitrary shear flow: 1) Construct the flow that is the even-periodic extension of the arbitrary shear flow. This requires extending the original domain by a factor of two. 2) For an arbitrary initial condition, include an image field initial condition that is equidistant from one of the two (closest) boundaries ($y = 0$ or $y = \pi$). 3) Restrict the analysis to only half of the (new) domain. This approach implies that the tracer satisfies Neumann boundary conditions.

The procedure above implies tracer solution with the triangular shear flow ($L_d = 1/2$) and the linear shear flow with Neumann (tracer) boundary conditions arise from the same eigenvalue problem (the EPs in the linear shear case are described in Doering & Horsthemke 1993). The location of the first EP in the linear shear flow described in Doering & Horsthemke (1993) does not match the location of the first EP of the triangular shear flow, but that can be explained by a rescaling of the domain M, which in turn shifts the value of k and Pe. The shifting of the EP locations also happens when the shear-flow periodicity P increases (from $P = 1$ to $P = 2$ or 3, as can be seen in the values of q_{cr} in Table 1).The equivalency between solutions to (2.2) for the triangular shear flow and the linear shear flow implies that tracer dispersion with the linear shear flow is strongly self-similar process in all its (shear dispersion) stages and, in the transient anomalous diffusion stage, can likely be model via a FFPE when the initial width is vanishingly small.

It is straightforward to apply the solution method in the presence of time-varying shear flows of the form (1.2), by discretely approximating piecewise constantly any arbitrary, bounded time-dependence in $U_0(t)$. This differs from the approach of Childress & Gilbert (1995) who restrict attention to time-periodic operators, i.e., to time-periodic velocity fields. In addition, the solution method in 2.2 can be applied also to the case of spatial and temporal variability in diffusivity $\kappa = \kappa(y, t)$, as long as the spatial functional dependence is integrable. In this scenario, the role of $d\kappa/dy$ is identical to the role of the advecting velocity.

The ability to compute analytical solutions for passive scalar tracers governed by (1.1) for spatially- and time- varying flows, and diffusivities $\kappa(y, t)$, has important consequences to the study and modelling of biogeochemical tracers. While the inclusion of reaction terms into (1.1) makes the resulting governing equation non-linear, our solution method can be exploited when the *operator splitting* approach is used to solve, via alternating Δt steps of advection-diffusion followed by pure reaction, the resulting advection-diffusion-reaction equation (see Wheeler & Dawson 1987; Rubio *et al.* 2008; Kulkarni & Lermusiaux 2019). Although outside of the scope of this study, employing our analytical approach when considering shear flows like those in (1.2) could result in the reduction of spurious mixing associated with numerical advecting schemes (see LeVeque 2002; Durran 2010).

5. Conclusions

The problem of passive scalar dispersion has been extensively studied, but only in a few ideal shear flows and in asymptotic parameter regimes (Taylor 1953; Aris 1956; Young *et al.* 1982; Rhines & Young 1983; Doering & Horsthemke 1993; Latini & Bernoff 2001; Camassa *et al.* 2010; Haynes & Vanneste 2014). Here, we present an Eulerian matrix method to compute analytical solutions to the tracer advection-diffusion equation for a broad class of velocity fields and initial conditions. We focus on steady, spatially-periodic laminar shear flows, and doubly periodic boundary conditions. But the method allows to compute solutions to time-varying flows that can be expressed as (1.2), with no-flux (tracer) boundary conditions in the cross-stream direction, and it applies to any shear flow that can be defined via a Fourier series (integrable).

The Eulerian matrix method calculates the eigenvalue spectra of the linear, non-self-adjoint operator of (1.1). We thoroughly describe the properties of the eigenvalue spectrum. In particular, the spectrum properties are shaped by Exceptional Points with implications for scalar mixing rates, and for the time evolution of localized tracer patches. The analysis also leads to along- and across- stream lengthscales that determine the effect of the shear.

The Eulerian matrix method is most efficient at low and intermediate Péclet numbers ($Pe < 10^4$), due to the iterative computation of eigenvalue-eigenfunctions. No formal restriction on the value of Pe applies, however. Also, the present method captures all the stages of shear dispersion. This method therefore complements other approaches that apply to very large Pe and/or to specific regimes of shear dispersion.

Appendix A. Analytical expressions of shear flow velocity profiles

Table 4 shows the analytical expressions and Fourier coefficients used in the definition on the main four shear flows in Fig. 2, and their explicit dependence on the inverse width parameter L_d. All the shear flows share the feature that their maxima are at $y = \pi$, their minima are at $y = \{0, 2\pi\}$, and they converge to a point shear flow as $L_d \to \infty$, defined as

$$U(y) = \begin{cases} 1, & \text{if } y = \pi \\ 0, & \text{otherwise.} \end{cases}$$

In the case of the polynomial shear flow, we extend it periodically from $-\pi < y < \pi$, so that within the interval $y \in [0, 2\pi]$ the velocity is maximum at $y = \pi$ and decays algebraically to zero at $y = \{0, 2\pi\}$. The Fourier coefficients for the polynomial shear flow are

$$\alpha_m = \frac{2}{\pi} \int_0^{\pi} \frac{y^{2L_d}}{\pi^{2L_d}} \cos(my)\, dy. \tag{A 1}$$

The simplest case $L_d = 1$ yields the quadratic (parabolic) shear flow, which has Fourier coefficients

$$\alpha_m = \frac{4(-1)^m}{m^2}. \tag{A 2}$$

Shear flow	Analytical Expression	Fourier Coefficients
Cosine	$1/2\left[1-\cos(y)\right]$	$\alpha_0 = -2\alpha_1 = 1$
Triangular	$U(y) = \begin{cases} 0, & \text{if} \quad y_1 < y < 2\pi \\ 2L_d\left(y_1 - y\right)/\pi, & \text{if} \quad \pi < y < y_1 \\ 2L_d\left(y - y_0\right)/\pi, & \text{if} \quad y_0 < y < \pi \\ 0, & \text{if} \quad 0 \leqslant y \leqslant y_0 \end{cases}$	$\alpha_m = \begin{cases} \frac{4L_d(-1)^m}{\pi^2 m^2}\left[1-\cos\left(\frac{m\pi}{2L_d}\right)\right], & m > 0 \\ 1/(2L_d), & m = 0 \end{cases}$
Square	$U(y) = \begin{cases} 1, & \text{if} \quad y_0 \leqslant y \leqslant y_1 \\ 0, & \text{otherwise} \end{cases}$	$\alpha_m = \begin{cases} \frac{2(-1)^m}{m\pi}\sin\left(\frac{m\pi}{2L_d}\right), & m > 0 \\ 1/L_d, & m = 0 \end{cases}$
Gaussian	$U(y) = \exp\left[-L_d^2(y-\pi)^2\right]$	$\alpha_m = \frac{(-1)^m}{L_d\sqrt{\pi}}\exp\left[-\left(\frac{m}{2L_d}\right)^2\right],\ m \geqslant 0$
Polynomial	$U(y) = y^{2L_d}/\pi^{2L_d}$	$\alpha_0 = \frac{2}{2L_d+1}$, see text for $m > 0$

TABLE 4. Analytical expressions for the flows considered in this study, their dependence on the inverse width parameter L_d, and their Fourier coefficients. For the triangular and square shear flows, the constants are $y_0 = \pi(2L_d - 1)/2L_d$ and $y_1 = \pi(2L_d + 1)/2L_d$.

When $L_d = 2$, the quartic polynomial has Fourier coefficients

$$\alpha_m = -\frac{8(-1)^m\left(\pi^2 m^2 - 6\right)}{m^4}. \tag{A 3}$$

Appendix B. Shift-reflect symmetry and Exceptional Points

The shift-reflect symmetry of the shear flow is a necessary condition for the presence of Exceptional Points (EPs). Consider the shifted Hill's equation (compare to (2.10))

$$\frac{d^2\phi_{2n}(\tilde{y}-\pi/2)}{d\tilde{y}^2} + \left[a_{2n} - 2qU^*(2\tilde{y}-\pi)\right]\phi_{2n}(\tilde{y}-\pi/2) = 0, \tag{B 1}$$

and the complex-conjugate of Hill's equation for the neighboring mode

$$\frac{d^2\overline{\phi}_{2n+2}(\tilde{y})}{dy^2} + \left[\overline{a}_{2n+2} - 2\overline{q}U^*(2\tilde{y})\right]\overline{\phi}_{2n+2}(\tilde{y}) = 0, \tag{B 2}$$

where the overline is the complex conjugate here. As $q = 2ikPe$ is purely imaginary, $-\overline{q}U^*(2y) = qU^*(2\tilde{y}) = -qU^*(2\tilde{y}-\pi)$, where the second equality follows for shear flow profiles that possess shift-reflect symmetry. This property makes equations (B 1) and (B 2) symmetric with respect to one another in the sense that their real parts are identical while their imaginary parts have opposite signs. Further, a shift-conjugate symmetry of the eigenfunctions is implied, which has the form $\phi_{2n}(\tilde{y}-\pi/2) = \overline{\phi}_{2n+2}$ (Ziener *et al.* 2012). Even for shear flows that are not shift-reflect symmetric, EPs can occur for sufficiently high modes. The reason is at sufficiently large modes (n value) the diagonal element of the nth row in (2.21) becomes purely real as the Fourier coefficient that appears in the diagonal decays monotonically.

Appendix C. Reference for variable names

The following Table 5 contains definitions of some of the most relevant variables of the main text.

Variable definitions	Symbols used
Non-dimensional domain aspect ratio. Sets the gravest streamwise mode that fits the domain. Arbitrary value. See eqn. (2.4)	$k_m = M/L$.
Non-dimensional shear flow width (Fig. 2)	L_d.
Normalized, arithmetic mean of fluid velocity (eqn 2.6)	$\alpha_0/2$.
Fourier coefficients that define an arbitrary (normalized) shear flow. See eqn (2.6)	$\alpha_m, m = 1, 2, \cdots$.
Normalized (pointwise) shear flow velocity minus the arithmetic mean	$U^* = U_0 - \alpha_0/2$
Periodicity of shear flow in y. See eqn. (2.7)–(2.8).	P ($P = 1$ default).
Dimensional amplitude of shear flow (arbitrary) used to normalized shear flow, and controls q eqn. (2.11)	U_0.
Even and odd eigenvalue-eigenfunction pairs, respectively. Each pair solves eqn. (2.10)	$\{\phi^e_{2n}, a_{2n}\}, \quad \{\phi^o_{2n+2}, b_{2n+2}\}, \quad n = 0, 1, 2\cdots$
Pure (modal) decay rate. See also (3.3)	$\overline{\sigma}$.
Smallest $q-$value at which $a_0(q)$ becomes complex. See Table 1.	q_{cr}.
Unique pre-factor to shear flow in effective diffusivity. See eqn. (3.5) and Table 2.	$\beta_2 = \sum_{m=1}^{\infty}(\alpha_m^2/(2m^2))$.
pth central moment. See eqn. (3.11)	$\mu_p(y, y)$.
Width of concentration.	$\mu_2^{1/2}(y, t)$.
Power law at which $p-$moment evolves via self-similar law. See eqn (3.13)	γ_p.
Scaling exponent of strongly self-similar processes. See eq. (3.14)	$\nu = p/\gamma_p$.

Table 5. Definition of relevant variables used throughout text.

Appendix D. Numerical validation

A side-by-side comparison between the analytical solution and a numerical simulation is given in Figure 11 for the case of a Gaussian initial condition in x that is uniform in y (section 3.2 with $\chi_y \to \infty$). Two velocity fields are shown: a wide triangular shear flow and a wide square shear flow. The model solves the advection-diffusion equation with the prescribed (steady) velocity field using a quasi-2nd order Adams-Bashforth explicit time-stepping scheme and a finite-volume method to calculate the spatial fluxes. The model uses a domain of size $-200\pi < x < 200\pi$, $0 < y < 2\pi$ with $N_x = 1280$ and $N_y = 128$ grid points. The dimensional parameters are $\kappa = 10^{-4}$ m^{2}s^{-1}, $M = 2\pi$ m, and the maximum velocity is $U_0 = 0.2$ ms^{-1}. These choices give $Pe = 2000$ with diffusive timescale $t_d = 1 = M^2/(4\pi^2\kappa) = 10^4$ s. The model is the open-source package Oceananigans (Ramadhan *et al.* 2020). As a simple speed comparison, the analytical solution evaluated at the same time-intervals as the stored model output was computed in under 3 minutes with

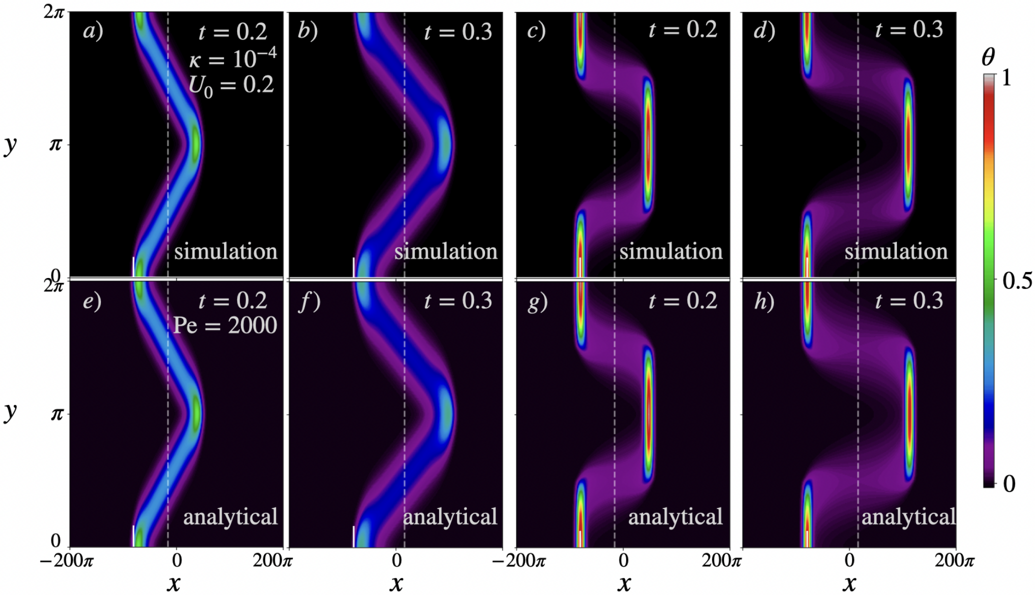

FIGURE 11. Comparison between numerical simulations (top row) and analytical solutions (bottom row). The velocity field is the wide triangular shear flow ($L_d = 1/2$, $P = 1$, left two columns) and the wide square shear flow ($L_d = 1$, $P = 1$, right two columns). The initial condition is uniform across the flow ($\Phi(2\tilde{y}) = 1$ in (2.37)) for better visualization and localized (Gaussian) around $x = -250$. The white dashed line represents the moving coordinate $x(t)$ that starts at $x(0) = -250$ and moves with the y-averaged flow. Both shear flows are shift-reflect symmetric so the tracer distribution $\theta(t)$ is symmetric (with a $\pi-$shift in y) with respect to the moving coordinate $x(t)$. Solid white lines at $x = -250$ and near $y = 0$ indicate the x location of the initial condition. The matrix truncation parameter $G = \sqrt{75}$. The numerical simulation results are from the Oceananigans package (Ramadhan *et al.* 2020).

a personal computer (even much less if only a single time-evaluation, say the final, is needed), whereas the simulation took several hours to perform.

The numerical model solves the tracer equations at center points, and our eigenvalue approach to solving (2.2) effectively calculates solutions at vorticity points on a C-staggered grid due to our domain (Fourier) mode decomposition (see Durran 2010 for more on grid types). Nonetheless, we interpolate the analytical solution to an equivalent centered grid (or interpolate the numerical solution to corner points), to further quantify the error evolution $\Delta\mathcal{E}$ over time. This is shown in Fig. 12 for the two flows in Fig 11, the error defined as follows

$$\Delta\mathcal{E}(t) = \sqrt{\frac{k_m}{4\pi^2}\int_0^{2\pi}\int_{-\pi/k_m}^{\pi/k_m}\left[\theta_a - \theta_b\right]^2 dxdy}, \tag{D 1}$$

where $4\pi^2/k_m$ is the area of the domain as a function of gravest mode k_m (see eqn. 2.4), and θ_a and θ_b represent the analytical and numerical solutions, interpolated onto a common spatial grid. We observe a small and bounded (mean-square) error over the entire tracer evolution (up to when the solution begins reentry due to periodic boundary conditions). A more complete analysis of the errors (e.g. as a function of grid refinement) remains outside the scope of this paper, but can be done to assess the convergence of discretized operators in two spatial dimensions.

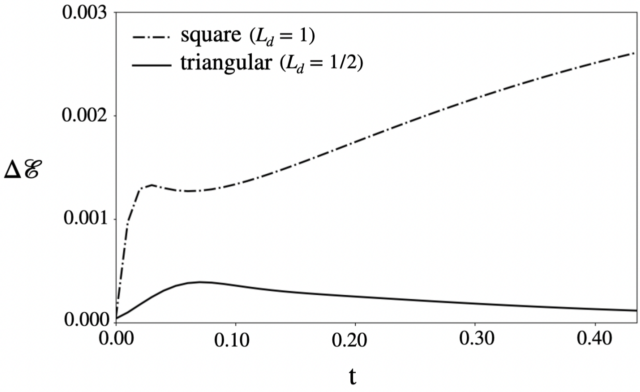

FIGURE 12. Error over time computed via (D 1) for the two flow solutions shown in Fig. 11. Time is non-dimensionalized by the diffusive timescale. The time span shown covers the case before the (tracer) solution begins reentry due to the periodic boundaries in the streamwise direction.

Lastly, we note that the error $\Delta\mathcal{E}$ is initially very small but non zero. This is because in the analytical solution there are spurious high frequency non-zero values (errors) typical of $\ll$ 1% of the solution amplitude largely uniformly distributed across the domain. These spurious values come from the non-zero cancellation in the triple sum (2.39), and arise from sensitivity to machine precision in the eigenspectra calculation of non-hermitian linear operators (non-normal matrices). Nonetheless, we found these spurious high-frequency tracer values associated to very high wavenumber behavior to decay similar to pure diffusion. For more on the subject of the effect of machine precision on spectra of linear non-Hermitian operators, we refer the reader to Trefethen 2005.

Appendix E. Gravest eigenvalue asymptotics at small q

The dependence of the gravest eigenvalue a_0 on q at small q can be easily approximated via regular asymptotic expansion. Following McLachlan (1947), consider small $|q|$ asymptotic approximations to $a_0(q)$ and $\phi_0(q,\tilde{y})$ of the form

$$a_0 \approx \beta_1 q + \beta_2 q^2 + \cdots , \tag{E 1}$$

$$\phi_0 \approx 1 + qC_1(2\tilde{y}) + q^2 C_2(2\tilde{y}) + \cdots , \tag{E 2}$$

where $C_1(2\tilde{y}), C_2(2\tilde{y}), \cdots$ are $\pi-$periodic functions and $\beta_1, \beta_2, \cdots$ are constant coefficients, all to be determined. Because $q = 2ikPe$ is purely imaginary, β_1 and β_2 determine the leading order terms of the imaginary and real components of the eigenvalue in the small q limit. From (E 1), (E 2), and the shear flow profile definition (2.6),

$$\phi_0^{''} = qC_1^{''} + q^2 C_2^{''} + \cdots , \tag{E 3}$$

$$a_0\phi_0 = \left[\beta_1 q + \beta_2 q^2 + \cdots\right]\left[1 + qC_1(2\tilde{y}) + q^2 C_2(2\tilde{y}) + \cdots\right] , \tag{E 4}$$

$$-2qU^*(2\tilde{y})\phi_0 = -2q\left[\sum_{m=1}^{\infty} \alpha_m \cos(2m\tilde{y})\right]\left[1 + qC_1(2\tilde{y}) + q^2 C_2(2\tilde{y}) + \cdots\right] . \tag{E 5}$$

Substituting into (2.10) and collecting powers of q gives the $O(q)$ equation

$$C_1^{''} + \beta_1 = 2\sum_{m=1}^{\infty} \alpha_m \cos(2m\tilde{y}). \tag{E 6}$$

As we are only interested in periodic solutions, $\beta_1 \equiv 0$. Integrating (E 6) yields $C_1 = -\sum_{m=1}^{\infty}(\alpha_m/(2m^2))\cos(2m\tilde{y})$. The $O(q^2)$ equation is

$$C_2'' + \beta_2 = -2\left(\sum_{m=1}^{\infty}\alpha_m\cos(2m\tilde{y})\right)\left(\sum_{m'=1}^{\infty}\frac{\alpha_{m'}}{2m'^2}\cos(2m'\tilde{y})\right). \tag{E 7}$$

The right hand side yields constant terms for $m = m'$ in the product of the two infinite series (like $2\cos^2(2\tilde{y}) = \cos(4\tilde{y}) + 1$). As C_2 is periodic, β_2 must exactly balance these constant terms on the right hand side. Therefore, the coefficient β_2 in (E 1) is given exactly by

$$\beta_2 = \sum_{m=1}^{\infty}\frac{\alpha_m^2}{2m^2}, \tag{E 8}$$

where α_m are the Fourier coefficients in the definition of the shear flow (2.6). This expression is used in the formula for effective diffusivity (3.5).

Acknowledgments. The authors would like to thank four anonymous reviewers for their criticisms, comments, and suggestions that greatly contributed towards the improvement of our manuscript. We also thank Dr. Ali Mani who suggested the potential role that Mathieu's equation with imaginary parameter plays in the solution to the initial value problem.

Funding. This project was funded by the Johns Hopkins University Institute for Data Intensive Engineering and Science Seed Funding Initiative and NSF grant 1835640.

Declaration of Interests. The authors report no conflict of interest.

Author ORCID. M. A. Jimenez-Urias, https://orcid.org/0000-0002-4583-1831; T. W. N. Haine, https://orcid.org/0000-0001-8231-2419.

Author contributions. M. Jimenez-Urias derived the analytical solution method, computed solutions, and performed the necessary simulations for comparison. Both authors contributed equally to analysing results, reaching conclusions, and in writing the paper.

REFERENCES

Antonsen Jr, Thomas M, Fan, Zhencan, Ott, Edward & Garcia-Lopez, E 1996 The role of chaotic orbits in the determination of power spectra of passive scalars. *Physics of Fluids* **8** (11), 3094–3104.

Aref, Hassan 1984 Stirring by chaotic advection. *Journal of fluid mechanics* **143**, 1–21.

Aris, Rutherford 1956 On the dispersion of a solute in a fluid flowing through a tube. *Proceedings of the Royal Society of London. Series A. Mathematical and Physical Sciences* **235** (1200), 67–77.

Arscott, Felix Medland 2014 *Periodic differential equations: an introduction to Mathieu, Lamé, and allied functions*, , vol. 66. Elsevier.

Bender, Carl M 1999 The complex pendulum. *Physics Reports* **315** (1-3), 27–40.

Bender, Carl M & Boettcher, Stefan 1998 Real spectra in non-Hermitian Hamiltonians having PT symmetry. *Physical Review Letters* **80** (24), 5243.

Biferale, L, Crisanti, A, Vergassola, M & Vulpiani, A 1995 Eddy diffusivities in scalar transport. *Physics of Fluids* **7** (11), 2725–2734.

Boano, Fulvio, Harvey, Judson W, Marion, Andrea, Packman, Aaron I, Revelli, Roberto, Ridolfi, Luca & Wörman, Anders 2014 Hyporheic flow and transport processes: Mechanisms, models, and biogeochemical implications. *Reviews of Geophysics* **52** (4), 603–679.

Brimacombe, Chris, Corless, Robert M & Zamir, Mair 2021 Computation and applications of mathieu functions: a historical perspective. *SIAM Review* **63** (4), 653–720.

Camassa, Roberto, McLaughlin, Richard M & Viotti, Claudio 2010 Analysis of passive scalar advection in parallel shear flows: sorting of modes at intermediate time scales. *Physics of Fluids* **22** (11), 117103.

Castiglione, P, Mazzino, A, Muratore-Ginanneschi, Paolo & Vulpiani, A 1999 On strong anomalous diffusion. *Physica D: Nonlinear Phenomena* **134** (1), 75–93.

Chaos-Cador, Lorea & Ley-Koo, E 2002 Mathieu functions revisited: matrix evaluation and generating functions. *Revista mexicana de física* **48** (1), 67–75.

Childress, Stephen & Gilbert, Andrew D 1995 *Stretch, twist, fold: the fast dynamo*, , vol. 37. Springer Science & Business Media.

Curtis, Christopher & Deconinck, Bernard 2010 On the convergence of hill's method. *Mathematics of computation* **79** (269), 169–187.

De Moura, Alessandro PS 2014 Strange eigenmodes and chaotic advection in open fluid flows. *Europhysics Letters* **106** (3), 34002.

Deconinck, Bernard & Kutz, J Nathan 2006 Computing spectra of linear operators using the floquet–fourier–hill method. *Journal of Computational Physics* **219** (1), 296–321.

Doering, Charles R & Horsthemke, Werner 1993 Stability of reaction-diffusion-convection systems: the case of linear shear flow. *Physics Letters A* **182** (2-3), 227–231.

Dubkov, Alexander A, Spagnolo, Bernardo & Uchaikin, Vladimir V 2008 Lévy flight superdiffusion: an introduction. *International Journal of Bifurcation and Chaos* **18** (09), 2649–2672.

Durran, Dale R 2010 *Numerical methods for fluid dynamics: With applications to geophysics*, , vol. 32. Springer Science & Business Media.

Eckart, Carl 1948 An analysis of the stffiring and mixing processes in incompressible fluids .

Elrick, DE 1962 Source functions for diffusion in uniform shear flow. *Australian Journal of Physics* **15** (3), 283–288.

Faller, Alan J & Auer, Stephen J 1988 The roles of langmuir circulations in the dispersion of surface tracers. *Journal of Physical Oceanography* **18** (8), 1108–1123.

Fereday, DR & Haynes, PH 2004 Scalar decay in two-dimensional chaotic advection and batchelor-regime turbulence. *Physics of Fluids* **16** (12), 4359–4370.

Ferrari, R, Manfroi, AJ & Young, WR 2001 Strongly and weakly self-similar diffusion. *Physica D: Nonlinear Phenomena* **154** (1-2), 111–137.

Giona, M, Adrover, A, Cerbelli, S & Vitacolonna, V 2004 Spectral properties and transport mechanisms of partially chaotic bounded flows in the presence of diffusion. *Physical review letters* **92** (11), 114101.

Haynes, Peter & Shuckburgh, Emily 2000 Effective diffusivity as a diagnostic of atmospheric transport: 1. stratosphere. *Journal of Geophysical Research: Atmospheres* **105** (D18), 22777–22794.

Haynes, PH & Vanneste, J 2014 Dispersion in the large-deviation regime. Part I: Shear flows and periodic flows. *arXiv preprint arXiv:1401.6665* .

Heiss, WD 1999 Phases of wave functions and level repulsion. *The European Physical Journal D-Atomic, Molecular, Optical and Plasma Physics* **7**, 1–4.

Heiss, WD 2004 Exceptional points of non-Hermitian operators. *Journal of Physics A: Mathematical and General* **37** (6), 2455.

Heiss, WD 2012 The physics of exceptional points. *Journal of Physics A: Mathematical and Theoretical* **45** (44), 444016.

Hernández, E & Mondragón, A 1994 The 2+ doublet in 8be: an example of accidental resonance degeneracy. *Physics Letters B* **326** (1-2), 1–4.

Hill, GW 1886 Mean motion of the lunar perigee. *Acta Math* **8** (1), 1.

Hunter, C & Guerrieri, B 1981 The eigenvalues of Mathieu's equation and their branch points. *Studies in Applied Mathematics* **64** (2), 113–141.

Ikebe, Yasuhiko, Asai, Nobuyoshi, Miyazaki, Yoshinori & Cai, DongSheng 1996 The eigenvalue problem for infinite complex symmetric tridiagonal matrices with application. *Linear algebra and its applications* **241**, 599–618.

Keating, Shane R, Kramer, Peter R & Smith, K Shafer 2010 Homogenization and mixing measures for a replenishing passive scalar field. *Physics of Fluids* **22** (7), 075105.

Kulkarni, Chinmay S & Lermusiaux, Pierre FJ 2019 Advection without compounding errors through flow map composition. *Journal of Computational Physics* **398**, 108859.

Latini, Marco & Bernoff, Andrew J 2001 Transient anomalous diffusion in poiseuille flow. *Journal of Fluid Mechanics* **441**, 399–411.

LeVeque, Randall J 2002 *Finite volume methods for hyperbolic problems*, , vol. 31. Cambridge university press.

Lighthill, MJ 1966 Initial development of diffusion in poiseuille flow. *IMA Journal of Applied Mathematics* **2** (1), 97–108.

Magnus, Wilhelm & Winkler, Stanley 2013 *Hill's equation*. Courier Corporation.

Majda, Andrew J & Kramer, Peter R 1999 Simplified models for turbulent diffusion: theory, numerical modelling, and physical phenomena. *Physics reports* **314** (4-5), 237–574.

McLachlan, N.W. 1947 *Theory and Application of Mathieu Functions*. Oxford University Press.

Meunier, Patrice & Villermaux, Emmanuel 2010 The diffusive strip method for scalar mixing in two dimensions. *Journal of fluid mechanics* **662**, 134–172.

Meunier, Patrice & Villermaux, Emmanuel 2022 The diffuselet concept for scalar mixing. *Journal of Fluid Mechanics* **951**, A33.

Miri, Mohammad-Ali & Alu, Andrea 2019 Exceptional points in optics and photonics. *Science* **363** (6422).

Neuman, Shlomo P & Tartakovsky, Daniel M 2009 Perspective on theories of non-fickian transport in heterogeneous media. *Advances in Water Resources* **32** (5), 670–680.

Olver, Frank W J, Lozier, Daniel W, Boisvert, Ronald F & Clark, Charles W 2010 *NIST handbook of mathematical functions hardback and CD-ROM*. Cambridge University press.

Ottino, Julio M 1990 Mixing, chaotic advection, and turbulence. *Annual Review of Fluid Mechanics* **22** (1), 207–254.

Pierrehumbert, Raymond T 1994 Tracer microstructure in the large-eddy dominated regime. *Chaos, Solitons & Fractals* **4** (6), 1091–1110.

Pierrehumbert, Raymond T 2000 Lattice models of advection-diffusion. *Chaos: An Interdisciplinary Journal of Nonlinear Science* **10** (1), 61–74.

Ramadhan, Ali, Wagner, Gregory LeClaire, Hill, Chris, Campin, Jean-Michel, Churavy, Valentin, Besard, Tim, Souza, Andre, Edelman, Alan, Ferrari, Raffaele & Marshall, John 2020 Oceananigans.jl: Fast and friendly geophysical fluid dynamics on gpus. *Journal of Open Source Software* **5** (53), 2018.

Rhines, Peter B & Young, William R 1983 How rapidly is a passive scalar mixed within closed streamlines? *Journal of Fluid Mechanics* **133**, 133–145.

Rubio, AD, Zalts, A & El Hasi, CD 2008 Numerical solution of the advection–reaction–diffusion equation at different scales. *Environmental Modelling & Software* **23** (1), 90–95.

Seeger, A 1997 Transverse spin relaxation of spin carriers diffusing in spatially periodic magnetic fields. *Hyperfine interactions* **105** (1-4), 151–159.

Seo, Il Won & Cheong, Tae Sung 1998 Predicting longitudinal dispersion coefficient in natural streams. *Journal of hydraulic engineering* **124** (1), 25–32.

Shaw, Tiffany A, Thiffeault, Jean-Luc & Doering, Charles R 2007 Stirring up trouble: multi-scale mixing measures for steady scalar sources. *Physica D: Nonlinear Phenomena* **231** (2), 143–164.

Smith, K Shafer 2005 Tracer transport along and across coherent jets in two-dimensional turbulent flow. *Journal of Fluid Mechanics* **544**, 133–142.

Strutt, MJO 1948 Xxx.—on hill's problems with complex parameters and a real periodic function. *Proceedings of the Royal Society of Edinburgh Section A: Mathematics* **62** (3), 278–296.

Sukhatme, Jai & Pierrehumbert, Raymond T 2002 Decay of passive scalars under the action of single scale smooth velocity fields in bounded two-dimensional domains: From non-self-similar probability distribution functions to self-similar eigenmodes. *Physical Review E* **66** (5), 056302.

Taylor, Geoffrey Ingram 1953 Dispersion of soluble matter in solvent flowing slowly through a tube. *Proceedings of the Royal Society of London. Series A. Mathematical and Physical Sciences* **219** (1137), 186–203.

Thiffeault, J-L 2008 Scalar decay in chaotic mixing. In *Transport and Mixing in Geophysical Flows*, pp. 3–36. Springer.

Trefethen, Lloyd N 2005 Spectra and pseudospectra: The behaviour of non-normal matrices and operators. In *The graduate student's guide to numerical analysis' 98: Lecture notes from the VIII EPSRC Summer School in Numerical Analysis*, pp. 217–250. Springer.

Van Sebille, Erik, Griffies, Stephen M, Abernathey, Ryan, Adams, Thomas P, Berloff, Pavel, Biastoch, Arne, Blanke, Bruno, Chassignet, Eric P, Cheng, Yu, Cotter, Colin J & others 2018 Lagrangian ocean analysis: Fundamentals and practices. *Ocean Modelling* **121**, 49–75.

Vanneste, J 2006 Intermittency of passive-scalar decay: Strange eigenmodes in random shear flows. *Physics of fluids* **18** (8), 087108.

Weeks, Eric R, Urbach, JS & Swinney, Harry L 1996 Anomalous diffusion in asymmetric random walks with a quasi-geostrophic flow example. *Physica D: Nonlinear Phenomena* **97** (1-3), 291–310.

Wheeler, Mary F & Dawson, Clint N 1987 An operator-splitting method for advection-diffusion-reaction problems. In *The Mathematics of Finite Elements and Applications VI*.

Young, WR, Rhines, PB & Garrett, CJR 1982 Shear-flow dispersion, internal waves and horizontal mixing in the ocean. *Journal of Physical Oceanography* **12** (6), 515–527.

Zaburdaev, Vasily, Denisov, Sergey & Klafter, Joseph 2015 Lévy walks. *Reviews of Modern Physics* **87** (2), 483.

Zel'dovich, Yakov Borisovich 1982 Exact solution of the problem of diffusion in a periodic velocity field, and turbulent diffusion. In *Doklady Akademii Nauk*, , vol. 266, pp. 821–826. Russian Academy of Sciences.

Ziener, CH, Rückl, M, Kampf, T, Bauer, WR & Schlemmer, Heinz-Peter 2012 Mathieu functions for purely imaginary parameters. *Journal of Computational and Applied Mathematics* **236** (17), 4513–4524.